REANALYSIS OF X-RAY EMISSION FROM M87 II: MULTIPHASE MODELS

John C. Tsai and Edmund Bertschinger

Center for Theoretical Physics, Center for Space Research,
and Department of Physics,
Massachusetts Institute of Technology

DRAFT

ABSTRACT

I. INTRODUCTION

In a previous paper (Tsai & Bertschinger 1992; hereafter TB), we showed that the hot intracluster gas around M87 could not be adequately explained in terms of a spherically symmetric, single phase model. (What we mean by a single phase model is that all of the intracluster gas at a given location is taken to be at a single temperature and density). Although this was a result that was expected on the basis of much previous work (Stewart et al. 1984; White & Sarazin 1988; and White et al. 1991), the incomplete use and subsequent revisions of the available data as well as modelling inaccuracies rendered the conclusions of these authors uncertain. We showed, however, that a complete treatment of the revised data did indeed result in the same conclusions. We found that although data from the *Einstein* satellite High Resolution Imager (HRI), Imaging Proportional Counter (IPC), and Focal Point Crystal Spectrometer (FPCS) could indeed be simultaneously explained by a single phase model, data from the Solid State Spectrometer (SSS) and optically determined mass estimates could not be similarly explained. A qualitative discussion was then given to indicate how the adoption of a specific multiphase model could plausible improve upon the single phase model, but a detailed discussion was delayed until the present paper.

Multiphase models for intracluster gas have been previously studied by a number of authors including Thomas, Fabian, & Nulsen (1987), White and Sarazin in a series of papers (White & Sarazin 1987a; 1987b; 1987c; and 1988), and White et al. (1991). In the first case, Thomas et al. investigated a model where an initial distribution of gas densities was assumed at large radius and then allowed to evolve self consistently towards the center of the cluster. Applying this model to a series of clusters, not including Virgo or Perseus, they found that the subsequent results agreed well with the previous single phase results of Fabian et al. (1981). Furthermore, the mass accretion rate, $\dot{M}(< r)$ was found to be approximately given by $\dot{M}(< r) \sim r$. White and Sarazin, alternatively, studied a multiphase model that was given by a "local" prescription whereby the rate at which gas cooled and consequently dropped out of the cluster was determined by local timescales. In this regard, they investigated the cases where the mass dropout rate was determined by

the local cooling time and the thermal instability timescale. This model was subsequently studied numerically where it was found that the flow structure was basically the same for the two choices of timescale and that the resulting distribution of accreted material was in general steeper than an isothermal mass distribution. When the cooling time model was applied to data from M87 and NGC 1275, it was found that the model provided a somewhat reasonable fit and that the mass cooling rate $\dot{M}(< r)$ was again approximately proportional to r, although a power law was not a very good fit to the actual mass accretion rate profile. Finally, White et al. found in a series of isothermal fits to SSS spectra of a number of clusters that an improved fit to the data was achieved by including a cooling flow component and an extra column density of absorbing material above the Galactic value.

In this paper we reanalyse the X-ray data for the gas around M87 in the same spirit as the work in TB. That is, by assuming several cooling flow models, we will try to improve upon the shortcomings of the investigations that we discussed in the previous paragraph. As stated in the Introduction of TB, these shortcomings render the conclusions of these previous papers rather uncertain. In the work of White and Sarazin (1988), for example, although some derived temperature information from the spectral instruments of *Einstein* were used to constrain the models, the predicted spectra for these instruments were not explicitly computed nor were they compared to the data. In addition, the degree of agreement of the models with the imaging data (which were used to fix the parameters of the model) is not quantified statistically nor is the agreement with the optically determined mass profiles. And finally, the instrument parameters that were used by the authors (White & Sarazin 1988), which were taken from Giacconi et al. (1979), have subsequently been revised (Harris 1984). The claim that the models are in good agreement with the data is, therefore, uncertain. With regard to the models of White et al. (1991), in the case of the gas around M87, the authors only used data from the SSS to constrain the models and, furthermore, only made isothermal fits with a temperature derived from wide field of view instruments. The agreement of the models with the available data from the other instruments is therefore unknown. In addition, since the central regions of the cluster are expected to be the coolest (Canizares et al. 1982; Lea et al. 1982), using the higher, field of view averaged temperature may ascribe too much of the low temperature emission to the cooling component of the gas.

In the present paper, we will adopt the procedure of TB and reanalyse the data in the following manner. We will first assume a multiphase model with which we can compute the surface brightnesses as seen by the HRI and IPC. We can, furthermore, compute the line fluxes of the lines seen by the FPCS and the mass profile after assuming hydrostatic equilibrium. The parameters of the model are then adjusted to fit the data. We will then check to see whether the resulting model is consistent with the SSS spectrum and the equivalent width of the 7 keV complex of Fe lines as seen by large field of view instruments (e.g. *EXOSAT*). Our aim then is to see whether, as we argued qualitatively in TB, the cooling flow models we pick will result in an improvement over the single phase case with respect to the goodness of fit to the data. One of the cooling flow models we will consider is just the cooling time model of White and Sarazin. This will enable us to confirm the findings of these authors with our more complete analysis using the revised instrument parameters. We will not consider the thermal instability model of these authors since it was shown from numerical computations (White & Sarazin 1987c) that the results were very similar to those of the cooling time model. We will, however, investigate an *ad hoc* power law model for the multiphase medium; that is, a model in which the mass accretion profile is assumed to be a power law. The motivation here is to examine alternatives to the "local" models of White and Sarazin which, as described above, resulted in mass accretion profiles that were not well fit by power laws. If we recall that the model of Thomas et al. (1987) (which we will not consider since it is somewhat more difficult to implement in the current analysis) did indeed result in mass accretion profiles that were relatively well fit by a power law, we can determine based on which of our chosen models gives the better fit whether the data favor the "local" models or some nonlocal model. (Note, however, that our power law models are still local in the sense that the mass drop-out rate is determined locally by the given power law; the resulting mass accretion profile nevertheless mimics those of Thomas et al. (1987)).

We will also try to confirm the findings of White et al. (1991) that a column density of absorbing gas above the Galactic value is required to improve the fit to the low energy part of the SSS spectrum. In TB, we have already shown that the inclusion of this extra column density without a cooling component does not result in a better fit of the models to the SSS data. In this paper, we will be able to consider this question in the more general context of the two previously mentioned cooling flow models. This will allow us to see

whether the additional spectroscopic and imaging data besides that from the SSS that we will include in our analysis can be consistently explained along with the SSS data when the column density of absorbing gas is taken to be larger than the Galactic value. This will be done by performing fits to the data assuming two possibilities for the distribution of the additional cool, absorbing gas. The first is to assume that the cool gas is distributed evenly across the cluster and that the corresponding column density does not vary with radius. This possibility is partially supported by the work of White et al. (1991). In addition to a pointing of the SSS centered on M87, these authors also used a pointing that was somewhat offset from the center. They found that the same additional column density was required in both cases. However, the two pointings were only separated by about 2.5′ which corresponds to a distance of only 11 kpc with an assumed distance to M87 of 15 Mpc. Hence the second, off center, pointing of the SSS does not give that much of an indication as to how the extra column density is distributed in radius. In fact, when the absorbing column density was allowed to float in the IPC spectral analysis of M87 (Fabricant & Gorenstein 1983), the derived value at radii larger than about 3′ was consistent with the Galactic column density. We will therefore additionally consider the possibility that the distribution of column density is a function of the projected radius. We chose to implement this radial dependence in a self consistent manner which will be described in the subsequent section on the Method of Solution.

For the remainder of this paper, we will assume that the distance to M87 is 15 Mpc. Where appropriate, we will indicate the dependence on this assumed distance by including the constant d_{15} in the result. We have defined $d_{15} = D_{M87}/15$ Mpc where D_{M87} is the assumed distance to M87. The outline for this paper is as follows. In section II, we present our method of solution where we describe the assumptions that we will make and the methods that we use to compare our models to the data. We will also briefly describe the data that will be used. In section III, we present the results for the cooling time multiphase model and the results of the power law cooling models will be described in section IV. We will present our derived mass accretion profiles in section V and we will draw our conclusions in section VI.

II. METHOD OF SOLUTION

We begin by stating our assumptions. First, we will suppose that the thermal emission from the intracluster gas around M87 comes from two distinct components. The first component, or phase is an ambient, non–cooling distribution of hot gas that is taken to be spherically symmetric, in ionization equilibrium, and describable by density and temperature profiles. It is this phase alone that we had previously investigated in detail in TB with regard to its consistency with the data. Having found that the inclusion of only this phase was inadequate for this purpose, we now assume the existence of a second phase. This consists of a given quantity of gas, at a given radius, cooling instantaneously and isobarically from the temperature of the ambient medium at that radius to zero. The emission from the cooling component is then added to the emission from the ambient medium to get the total emission from the cluster. We note that in keeping with the assumption of spherical symmetry, we will also assume that the rate at which gas cools in the second component is a function only of the radius from the center of the cluster. Also, we will used the atomic emissivity code of Raymond (1989; private communication) in our models.

As stated in the Introduction, a multiphase medium model of this variety was previously investigated by White & Sarazin (1988) for the gas around M87 and NGC 1275 in Perseus. A discussion was given in this paper and an earlier paper (White & Sarazin 1987a) which provided the justification for the assumptions that we have adopted for the cooling phase. For example, the assumption of isobaric cooling was shown to be reasonable because the cooling flows were thermally unstable with the fastest growing linear modes being isobaric. Furthermore, even when the perturbations became nonlinear, their evolution was still isobaric as long as the temperature was greater than about 10^6 °K. Since most of the emission in X–rays arise at temperatures higher than this, we can conclude that the cooling component will cool isobarically in general. In addition, since most of the X–ray emission arrises at temperatures higher than 10^6 °K, even in the cooling component, it is still valid to use an ionization equilibrium code, such as that of Raymond (1989; private communication), to compute the X–ray emission. We will not discuss the validity of the other assumptions further as this issue is considered in the work of White and Sarazin. In addition, the assumptions that have adopted with regard to the ambient, non–cooling, medium have been discussed in section III of TB.

We now further assume, as in TB, that the density and temperature profiles of the ambient medium are parameterized by the forms

$$n_e(r) = n_0 \frac{(r/a_1)^{-\alpha_1}}{1+(r/a_1)^{\alpha_3}} \tag{1}$$

and

$$T(r) = T_\infty \left(\frac{r}{a_2+r}\right)^{\alpha_2} \tag{2}$$

where n_e is the electron number density. We have adopted the more generalized version of the density parameterization (ie. eq. (17) of TB) since it will allow more flexibility in the density profile at small radius as compared to the more restricted parameterization with α_3 fixed to unity. (This point is more extensively discussed in TB with regard to single phase fits but the analysis is also valid in the present case). The appropriateness of these profiles for use in the present study have been discussed in TB, as has the computation of the emission from this component of the gas as seen by the various *Einstein* instruments.

In the case of the cooling component, once the rate at which mass cools and drops out of the flow at any radius is specified, the corresponding emission from this component can also be computed. More specifically, if $\dot{\rho}(r)$ is the mass dropout rate in units of g/s/cm^3 at radius r, then the emissivity in the energy band from E_1 to E_2, $\epsilon^{\rm cool}_{E_1\rightarrow E_2}$, of the cooling component will be given by

$$\epsilon^{\rm cool}_{E_1\rightarrow E_2} = \frac{5}{2}\frac{k}{\mu m_p}\dot{\rho}\int_0^T \frac{\Lambda_{E_1\rightarrow E_2}(T')}{\Lambda(T')}dT' \tag{3}$$

where $\Lambda_{E_1\rightarrow E_2}$ is the atomic emissivity in the energy interval E_1 to E_2 and Λ is the bolometric emissivity, both in units of ergs cm^3/s. The quantity T is the temperature of the ambient phase at the given radius, k is the Boltzmann constant and μm_p is the mass per particle. The units for $\epsilon_{E_1\rightarrow E_2}$ are according ergs/s/cm^3.

The emission due to this component as seen by the *Einstein* instruments can now be easily computed again by applying the appropriate effective areas and response functions to the predicted emission. What must first be determined, however, is $\dot{\rho}$. In the case of White and Sarazin where this quantity is determined by the local cooling time, t_c, we have from equation (11) of White & Sarazin (1987a) that

$$\dot{\rho} = q\frac{\rho}{t_c} \tag{4}$$

where q is a parameter that determines the "efficiency" with which the cooling time mass drop-out occurs. Here, we have the definition

$$t_c = \frac{5}{2}\frac{\rho\frac{kT}{\mu m_p}}{n_e n_p \Lambda} \tag{5}$$

where n_p is the number density of protons and ρ is the average mass density. Inserting eqs. (4) and (5) into eq. (3), we see that the emissivity of the cooling component assuming the cooling time model is given by

$$\epsilon^{\rm cool}_{E_1\rightarrow E_2} = n_e n_p \Lambda_{E_1\rightarrow E_2}\frac{q}{T}\int_0^T \frac{\Lambda_{E_1\rightarrow E_2}(T')}{\Lambda(T')}dT' \tag{6}$$

where again T is the temperature of the ambient medium.

Now, in the case of the power law model, we simply take

$$\dot{\rho} = N_{\rm mult}\, r^{-\alpha_{\rm mult}} \tag{7}$$

which gives an emissivity in the energy band from E_1 to E_2 of

$$\epsilon^{\rm mult}_{E_1\rightarrow E_2} = \frac{5}{2}\frac{k}{\mu m_p}N_{\rm mult}\, r^{-\alpha_{\rm mult}}\int_0^T \frac{\Lambda_{E_1\rightarrow E_2}(T')}{\Lambda(T')}dT' \tag{8}$$

For given values of the new parameters associated with the cooling component (q in the case of the cooling time model, $N_{\rm mult}$ and $\alpha_{\rm mult}$ in the power law model), the emission can be computed. In performing our fits to the data, we simply add these parameters to those associated with the ambient medium and vary them in a χ^2 analysis. Before we describe exactly how this will be done, we first note that the data that we use in this paper will be precisely the same as that of TB. Since an in depth discussion was given in that paper, we refer the reader to sections II and III of TB for the details. We simply state that the HRI data that will be used is from Feigelson (1991; private communication), the IPC data is from Fabricant (1991; private communication), the FPCS data is from Canisares et al. (1982), and the SSS data and instrument parameters are taken from the *EXOSAT* data base. (Note that our response matrices have therefore been corrected for ice obscuration of the SSS aperture.) Furthermore, we will use the 7 keV equivalent width result from the *EXOSAT* observation of Edge et al. (1988) to constrain the metal abundances.

In performing our fits to the data, we will follow the treatment of TB with respect to the elemental abundances. We will first fix the relative abundances of the metals other than oxygen to be the solar values (Allen 1973). We will then fix the overall abundance to an initial guess and perform the fit to the data. The equivalent width of the 7 keV complex will then be computed from the resulting model and compared to the measured value. The overall metal abundance will then be adjusted accordingly and the fit to the data redone. Again, the 7 keV equivalent width will be computed and compared to the data. This process will be iterated until agreement with the observed value is achieved. In each of the aforementioned fits to the data, we will allow the abundance of oxygen to be parameter of the fit. This is because it will be determined by the fit primarily from the ratio of the observed fluxes of the OVIII Lyα line and the various iron lines as seen by the FPCS.

We will also treat the parameters of the fit in almost the same manner as in TB. First, the parameters associated with the density profile are a_1, α_1, α_3, and n_0 and the parameters associated with the temperature profile are a_2, α_2, and T_∞. (Recall that there will be the additional parameters from the cooling component; either q or N_{mult} and α_{mult}). As in TB, we will allow a_1, α_1, and n_0 to vary as parameters of the fit but we will impose the constraint that α_3 be fixed by the relation

$$\alpha_3 = 1.36 - \alpha_1 \tag{9}$$

The reason for this is again that we are only using IPC data out to 30' although data exists out to a radius of about 100'. We try to incorporate the information contained in the outer, unused IPC data by noting that the surface brightness profile is basically a power law with a well defined slope. Since the gas in this region is expected to be rather isothermal and since the emissivity at the temperatures expected in this region are relatively constant with temperature (this is true even with the addition of a cooling component; see Figure 31 of TB), the density profile in this region much then also be a power law with a slope that is specified by the slope of the surface brightness profile. Now, the slope at large radius of our density profile as parameterized in eq. (1) will be $-\alpha_1 - \alpha_3$) which must then equal the fixed slope as determined from the IPC surface brightness profile, which is 1.36. In addition, since that temperature of the gas at large radius is not well determined by the available data (see section II of TB), we will first fix T_∞ to be 3.8×10^7 °K and allow the

other parameters associated with the temperature profile to vary with the fit. It will turn out that we will have to modify this part of our procedure below because the resulting temperature profiles from a fit with a fixed T_∞ is inconsistent with spectral data from the IPC. This aspect of the fit constitutes a departure from the procedure of TB which we will describe below in section III.

One further departure from the methods of TB is that we will include in our fit to the data constraints from optical determinations of the mass profile from Sargent et al. (1978). The reason for this is so that there will be some weight assigned in the fitting process to getting the predicted mass as close as possible to the observed mass. The data are indicated in Figure 8 as the disks with error bars. Also indicated in this figure are the alternative determinations of Mould et al. (1987) (the dark solid line) and Huchra & Brodie (1987) (the square with error bar) from globular cluster data. These latter two mass estimates will not be used in our fitting since they are very discrepant for reasons that are not altogether clear. To compare our model predictions with the Sargent et al. data, we first assume hydrostatic equilibrium and use the hydrostatic equation (eq. (16) of TB) to compute the mass profile. However, this procedure is only valid in the region where hydrostatic equilibrium is a good assumption. In this regard, Fabricant et al. (1980) have shown that the freefall time is much shorter than the cooling time for radii outside of 5' implying that hydrostatic equilibrium is a good assumption in this region. In addition, Bertschinger (1989) has estimated that the sonic radius is inside of 1 kpc implying that hydrostatic equilibrium is probably a good assumption outside of this much smaller radius. We have therefore chosen to include only the 7 outermost data points from the determinations of Sargent et al. in our fitting and to disregard the rest of the data. These other data lie in a region where we cannot be certain that mass predictions based on the the hydrostatic equation will be accurate. We note that error bars in the data of Sargent et al. include only the purely statistical errors associated with the measurement of the velocity dispersions of the stars in M87.

As stated in the Introduction, with our more complete analysis of the data, we will re–evaluate the evidence for the presence of additional absorbing gas in the cluster. This will be done by first assuming that the value for the absorbing column density quoted by White et al. (1991) applies uniformly across the cluster. We will then determine if the fit to the low energy part of the SSS is correspondingly improved over the case where only

the Galactic value is assumed. In addition, since there is evidence based on the discrepant values of the column density determined by the SSS and IPC (see section III.(d) of TB), the possibility exists that the column density varies with radius from the center of M87. We can test this possibility by assuming a radial distribution for the column density and then again seeing if the results of a fit to the data will give a corresponding better prediction of the SSS data relative to the nominal case. This procedure can be implemented in several ways depending upon how we choose to distribute the extra column density. Here, we will perform a "self consistent" analysis where we assume that the additional absorption is due to gas that originated from the cooling flow itself and, therefore, has a column density determined by the properties of the flow. If we assume that the rate at which mass drops out of the flow $\dot{\rho}$ has not changed over the lifetime of the cluster and if we assume that the cooling gas falls ballistically towards the center of the flow along radial orbits with an initial velocity of zero, it can be shown (see for example the Appendix of White & Sarazin 1987c) that the density distribution of the cooled gas is given by

$$\rho_c(r) = \frac{1}{r^2} \int_r^{R_{max}(t_{max})} \frac{r_0^2 \ \dot{\rho}(r_0)}{\sqrt{2(\phi(r_0) - \phi(r))}} \ dr_0 \qquad (10)$$

where $\dot{\rho}$ is again the mass dropout rate given by either eq. (4) or eq. (7), r_0 is the radius at which the gas drops out of the ambient medium, r is the radius at which the density of cooled gas is to be determined and ϕ is the gravitational potential. The radius $R_{max}(t_{max})$ is the maximum radius from which matter could have dropped out and had time to reach the smaller radius r in the lifetime of the cluster t_{max}. R_{max} can also be computed implicitly from the potential by the relation

$$t_{max} = \int_r^{R_{max}} \frac{dr_0}{\sqrt{2(\phi(R_{max}) - \phi(r_0))}} \qquad (11)$$

The parameter t_{max} is fixed for any given fit to the data but, since it is not a well determined number, we will consider several fits with different values of this parameter in order to understand the effects of varying the cluster lifetime.

In eqs. (10) and (11), the potential is computed by an integration assuming the total mass $M(r)$ that is derived from the equation of hydrostatic equilibrium (eq. (16) of TB):

$$\phi(r) = \int_{r_{min}}^{r} \frac{GM(r')}{r'^2} \ dr' \qquad (12)$$

where r_{min} is some arbitrary minimum distance. Since all of our evaluations involve differences in the potential, this minimum distance can be arbitrarily chosen. Now, eq. (12) will not give an accurate value of the potential when hydrostatic equilibrium breaks down. However, this happens only at very small radii, as discussed above, and in our computations of ρ_c we have most of the contribution to the integral in eq. (10) coming from larger radii because of the factor of r_0^2. Problems with the computation of the potential at small radii will therefore not have a large effect on the evaluation of ρ_c.

The extra absorbing column density can now be easily computed as a line of sight integration of ρ_c. In order to do the computation, however, in addition to an unknown cluster lifetime, there is also an unknown fraction of the gas that becomes absorbing. In our subsequent fits, we have chosen this fraction to be unity, although we will demonstrate that a smaller value will not effect our conclusions. Finally, we note that our procedure of including extra absorption does not introduce additional parameters into the optimizations that are required.

III. RESULTS OF COOLING TIME MODEL

a) Results with a Galactic column density

In this section we present the results of fitting the cooling time models to the data. In order that we may better understand the manner in which the inclusion of an additional phase effects the conclusions, we will also initially present single phase fits to the data including constraints from the mass data. These latter fits are different from those presented in TB in that mass constraints are explicitly included in the fitting process. We first adopt a fixed value for T_∞ of 3.8×10^7 °K and assume that the abundance of the elements other than oxygen is 0.7 times solar. (This specific abundance of iron was picked based on work of TB where it was found that with this abundance and an oxygen abundance of about a few times higher, the 7 keV equivalent width was within the 1 σ error bar of the observation). We will further assume for this section that the column density of absorbing gas is fixed at the Galactic value of 2.5×10^{20}cm^2 (see section III.(d) of TB for a discussion and references).

The density and temperature profiles that result from the above fits to the data are presented in Figures 1 and 2 respectively. The dotted line gives the profiles in the case

where a single phase is assumed and the solid line corresponds to the case where the cooling time multiphase model is assumed. The best fit value for the efficiency of gas cooling out of the flow in the multiphase case is $q = 0.72$. (The short dashed lines of Figures 1 and 2, which are to be discussed later, correspond to a fit to the data where a higher value of T_∞ is assumed). Now, it turns out that the profiles shown in Figures 1 and 2 do not represent a satisfactory fit to the data for reasons that will be explained below. (What is done to address these shortcomings will also be presented below). Therefore, we will not consider in any detail the properties of these fits. We will, however, first consider here the way that the dropout efficiency parameter q will be treated in our fits. As was explained in section II, q is simply included as an additional parameter of the fit and will, therefore, not depend upon the radius. Hence, in the cooling time model, all of the radial variation in the mass dropout rate $\dot{\rho}$ comes from the radial dependence of the gas density and the cooling time. This is different from the treatment of White & Sarazin (1988) who adopted a general deconvolution technique that resulted in a radially varying value for q. In fact, in their deconvolutions, the value of q varied by over 2 orders of magnitude. This would seem to imply, therefore, that the radial dependence of the gas dropout rate has not been well parameterized by the cooling time model and that the radial dependence has to be contained in variations in q. A more appropriate test of how well the cooling time model matches the real dropout rate is therefore to assume that the efficiency remain a constant with radius. One may as well dispense with the cooling law in favor of some *ad hoc* law for $\dot{\rho}$ if much of the radial variation is contained in q.

We now return briefly to Figures 1 and 2 to describe some of the features of these profiles. The first thing to notice is that the density profile of the multiphase case (the solid line) lies everywhere below that of the single phase fit (the dotted line) but the two are otherwise similar in shape. The lower multiphase phase density arises simply because, at any given radius, the cooling component contributes additional emission to the gas thereby requiring a lower density to provide the same total emission as the single phase case. The temperature profiles are also similar in the two cases in that they are both close to relatively flat power laws, and the single phase case has slightly higher temperatures at large radius as compared to the multiphase case. The flatness of the temperature profiles is expected from our qualitative arguments in TB. It was shown that the predicted mass profiles from single phase models that were fit to the X-ray data fell below the optical estimates of Sargent et

al. (1979). It was then argued that this was due to both the low temperatures required at small radii and the significant value of the logarithmic derivative of the temperature with respect to radius. In the present case, having included constraints from the optical mass determinations in the fitting, we have, in effect, forced the temperatures profiles higher at small radius.

The issue that makes these fits unacceptable is the temperatures in the region from 3′ to about 30′. Based on the spectral response of the IPC, Fabricant & Gorenstein (1983) were able to place bounds on the temperature in this region and found that the gas was fairly isothermal. In addition, the SSS determination of the temperature at 7′ (Lea et al. 1982) gave a value that was consistent with the findings of the IPC authors. At about a radius of 10′, Fabricant and Gorenstein find a temperature of between about 3 keV to 5.5 keV. By looking at Figure 2, we see that the temperatures that correspond to our multiphase fit are well below these bounds and are discrepant with this data. In fact, since Fabricant and Gorenstein did not include emission from a possible cooling component in their analysis, we can not be sure of the exact degree of disagreement. We have therefore taken the best fit model, the density and temperature profiles of which are displayed as the solid lines of Figures 1 and 2, and computed the emission into each of the 15 pulse height channels of the IPC and found that we overproduce the count rate in the lowest energy channels and underproduce the count rate in the higher energy channels thus indicating that indeed the temperature is too low in our models. There is, however, still considerable uncertainty as to the exact temperature in the region under consideration because of two more recent observations. By scanning the region around M87, the temperature distribution was determined by both *EXOSAT* (Edge et al. 1988) and *GINGA* (Koyama et al. 1991). For radii less than about 30′, both instruments again determined that the gas was basically isothermal (although it was determined from *GINGA* that the temperature rose rather dramatically outside of about 1.5° but this is in some dispute (Edge 1991; private communication), however, the temperature determined by *EXOSAT* was about 2.5 keV and was about 2.2 keV from *GINGA*. The small size of the error bars quoted by the authors for both of these measurements (on the order of 10% for *EXOSAT* and 2% for *GINGA*) implied that their results were discrepant with those of the IPC. The disagreement, however, is not quite as bad as initially indicated. Since the assumed abundances in the various studies differed, the results must be compared

more carefully. The work with the *EXOSAT* and *GINGA* satellites used metal abundances of about half solar, whereas Fabricant and Gorenstein assumed solar abundances. These latter authors derive a temperature range of from about 2.5 keV to 3.8 keV in the region from 3′ to 6′ if half solar abundances are instead assumed. Therefore, the lower bound of the IPC results agrees with the determinations from *EXOSAT* but is still discrepant with those from *GINGA*. The exact temperature in these regions must therefore await measurements from future instruments with good spectral resolution and reasonable imaging capabilities, such as ASTRO-D, for example.

Even if we were to accept the lowest measured temperature from *GINGA*, however, our current temperature profile is still too low. We have tried to improve the situation by setting T_∞ to the higher value of 6×10^7 °K and redoing the fit. The resulting density and temperature profiles are shown as the short dashed lines of Figures 1 and 2. We see that although the temperature becomes somewhat larger, we still do not have agreement with the spectral data in that region. We have therefore adopted a different approach that will guarantee that the temperature restrictions are satisfied by the fit. Instead of fixing the parameter T_∞ to a given value during the fitting process, we will now allow it to vary but in a very restricted fashion. We will impose the restriction on our profiles that at a radius of 10′ the temperature must be 2.5 keV or about 2.9×10^7 °K. Furthermore, we will restrict the temperature to be less than 4×10^7 °K at a radius of 30′ in order that the "average" cluster temperature does not get too high and, therefore disagree with the relatively low temperatures as determined by wide filed of view instruments such as OSO-8 (Serlemitsos et al. 1977; Mushotzky et al. 1978; Rothenflug and Arnaud 1985). Therefore, for given values of the parameters a_2 and α_2, T_∞ is determined by the condition we impose at 10′.

In Figures 3 through 9, we now show the results of fits to the data having adjusted our fitting procedure to that described above. In Figures 3 and 4, we show the density and temperature profiles that result for a single phase fit (the dotted line) and a multiphase, cooling time model fit (the solid lines). Again notice the fact that the multiphase density lies below that of the single phase case again for the reason that that there is more emission coming out per unit volume with the inclusion of a cooling component. In Figure 4, we have also included for comparison the temperature profile that results from a multiphase fit with fixed T_∞ (long dashed dotted line; repeat of the solid line of Figure 2). We now pause to make some comments about the temperature profiles that we derived here and

in the subsequent fits of this paper. In Table 1, we will list the best fit parameters for the various fits presented here. The various cases will be labelled by the same letter as the panels that show the corresponding FPCS residuals (see below). If we, as a preview, refer to the table, we see that the core radii for the temperature profiles a_2 in all the fits are extremely large. This is by no means a statement that the physical core radius is as large as 10^{10} kpc. Rather, because of our assumed parameterization of the temperature, if the temperature profiles in the region that we are considering are very close to pure power laws, a very large core radius is indicated (see eq. (2)). For example, the present temperature profiles that are shown in Figure 4 are indeed basically pure power laws with radius and it will turn out that all the other temperature profiles will be very close to power laws as well. Again, why these profiles come out this way was discussed above. Specifically, the inclusion of constraints from the optical mass determinations required higher temperatures in the central regions over fits that did not include these constraints.

The total χ^2 for the single phase fit of Figures 3 and 4 is 82 for 42 degrees of freedom and the total χ^2 for the cooling time model fit is 78 for 41 degrees of freedom (7 HRI points, 26 IPC points, 8 FPCS lines, and 8 mass points, minus 7 parameters, 5 associated with the density and temperature profiles, the variable abundance of oxygen, and the efficiency factor q associated with the cooling component). In the multiphase case, the best value for q is 0.87 and the best fit abundance of oxygen is 2.7 times solar. We can apparently conclude that the single phase case gives a poor fit to the data (as we expected from TB) and that the cooling time model does not significantly improve upon the single phase case (the fit is still at about 4 σ off the best fit case). We must, however, examine the various contributions to the total χ^2 to better understand the effect of adding the the cooling component to understand whether there is any real improvement. This is done in Figures 5 through 8. For convenience in the discussion, we first describe the contents of these figures and then analyse them jointly.

In Figures 5 and 6, we plot the predicted HRI and IPC surface brightness distributions, respectively for the single phase fit (dotted lines) and for the cooling time model fit (solid lines). The data are plotted as the points with error bars. We see immediately that the fit to the IPC data looks good in both cases (contribution to χ^2 of 29 for 26 data points for the single phase case and 32 for the multiphase case) but that the fit to the HRI is not very good (contribution to χ^2 of 15 for 7 data points for the single phase fit and 18 for

7 data points for the multiphase case). Furthermore, the major contributors to χ^2 come from the innermost point and the second and third outermost points. This latter fact is not surprising since the same points are also the major contributors to the χ^2 in the single phase fits without mass constraints that we considered in TB.

Figure 7 shows the contribution to χ^2 due to the FPCS lines. For the eight lines considered, we plot the values of the observed flux minus the predicted flux divided by the error. The various lines are plotted along the horizontal axis with 1 referring to the OVIII Lyα line, 2 through 7 referring to the line blends one through six, respectively, and number 8 referring to the FeXVII line. The panels are labelled by a letter in the upper right hand corner and the total contribution to χ^2 from the lines is given in the lower right hand corner. Panel (a) gives the results of the single phase fit and panel (b) corresponds to the fit with the cooling time model. We see first of all that the fit to the lines in the single phase case is very poor. This is to be expected based on our work in TB where it was shown that the a good fit to the X-ray data implied a poor fit to the mass data. In the present case, the explicit inclusion of mass constraints during the fitting gives an improved fit to the mass data (Figure 8; see below) but significantly degrades the fit to the FPCS lines. In fact, the distribution of the residuals for the lines now resembles that of the fit to only the continuum X-ray data as shown in panel (h) of Figure 14 in TB. The lower temperature lines and line blends are underproduced by the models whereas the higher temperature lines are overproduced. From panel (b), we see that the adoption of the cooling phase dramatically improves the fit to the lines and that the distribution of the residuals now looks reminiscent of the single phase fit to the X-ray data without mass constraints (panel (i) of Figure 20 of TB). As we discussed qualitatively in TB, the assumption of the multiphase medium has allowed more of the emission due to the coolest lines observed by the FPCS to arise at the higher temperatures required to adequately fit the mass data. Again, this is because even if the ambient medium is at a temperature that is above the peak emissivity temperature of the lines, the gas will cool through the range of temperatures where the lines fluoresce.

In Figure 8, we show the mass profiles that correspond to our models when the assumption of hydrostatic equilibrium is adopted. These are plotted along with optical determinations of the mass by a series of authors. As we mentioned in the previous section, we indicate the mass determinations of Sargent et al. (1978) from spectroscopic

studies of M87 as the round data points with error bars, the result of Mould et al. (1987) from M87 globular clusters as the the heavy solid line, and the determination of Huchra & Brodie (1987), also from globular clusters, as the square data point with error bars. The dotted line gives the mass profile corresponding to the single phase fit, the solid line gives the profile corresponding to the cooling time model, and the dashed dotted line is the mass profile of a single phase fit to only the X-ray data, which is reproduced from TB for purposes of comparison. We now note several aspects of this figure. First, the goodness of fit to the mass data of Sargent et al. is basically the same in the single phase case as in the multiphase case (contribution to χ^2 of 15.2 for 7 data points in the single phase case and 16.6 in the multiphase case) and is rather poor for both cases. Also in both cases, the majority of the residuals come from the two outermost points. We note further that our derived mass profiles are consistent with the determination of Mould et al. to within about 20% over the range of radii given by these authors. In comparison, the profile corresponding to the single phase fit without mass constraints lies well below all of the optically derived mass points. Finally, our profiles are inconsistent with the determination of Huchra and Brodie by about a factor of 6. In order for our profiles to actually agree with this data, assuming that the density profile and the slope in the temperature profile remains unchanged, the temperature at this radius would have to be correspondingly increased by a factor of about 6. By consulting the temperature profiles in Figure 4, the resulting temperature would have to be about 13 keV which is well above any estimate for the temperature at this radius. This would apparently imply, unless the true temperature and density profiles are significantly different from our model profiles, that the determination of Huchra and Brodie are inconsistent with the X-ray data.

Having described and discussed the contents of Figures 5 through 8, we now give an analysis of the the general quality of the fit of our models to the data as well as the effect on the fit of adding the cooling component to the single phase model. Since we are mainly concerned with the fit of the multiphase case, we will not consider the single phase case any further here. Now, for the cooling time model, as we noted above, the contributions to χ^2 due to the FPCS lines and those due to the IPC part of the data indicate a fairly good fit to the data. However, the fit to the mass and HRI parts indicate a poor fit. We now first consider the IPC and FPCS parts of the fit. In the case of the IPC, the data are relatively straightforward to understand and use in the following sense. The sources

of emission other than that due to the thermal bremsstrahlung emission are relatively absent in this part of the cluster. Furthermore, point sources have been removed and the circularity of the X-ray isophotes indicate that the assumption of spherically symmetry is probably acceptable. Furthermore, the error bars are relatively well understood and can be used directly in a χ^2 fit. We conclude therefore that the value of χ^2 gives good statistical information regarding the goodness of fit to the data. In the case of the FPCS data, things are again relatively straightforward in the sense that the error bars that have been used are the purely statistical errors and the data should not be very significantly contaminated by sources other than the thermal bremsstrahlung emission. The contribution to χ^2 from these lines should therefore also give statistically meaningful information about the quality of the fit.

We now turn our attention to the HRI and the mass part of the data. For the mass part of the fit we see that there are overlapping optical determinations at the location of the outermost mass points of Sargent et al. In fact, the globular cluster determination of Mould et al. (solid line) at this location is inconsistent with the values of Sargent et al. and indicate that the mass should be somewhat higher. Taking this as an uncertainty in the value of mass at this location, we can consider the effects of excluding the contribution to χ^2 of the two outermost points of Sargent et al. For the five remaining data points, the total contribution to χ^2 would then be about 5, indicating a very good fit. We can therefore conclude that because of the uncertainty in the optical determinations at a radius of about 1', it is in fact possible that the predicted mass profile from our model is actually in very good agreement with the real mass profile. This is in contrast to our original conclusion that owing to the large contribution to χ^2 from the mass data, a poor fit was necessarily indicated. In order to come to a definitive conclusion about this part of the data therefore, we must wait for additional, independent determinations of the mass profile in this region. Note, however, that a modification of the mass data at this radius will not effect our conclusions on the single phase fits.

In the fit to the HRI data, we can first compare the present results to those of the single phase fits in TB where mass constraints were not included. Recall that in this latter case, it was a found that an acceptable fit to the entire X-ray data set was obtained. We can therefore compare the residuals in the HRI part of the fit for the acceptable single phase fit (see Figure 12 of TB) and the multiphase fit. From this we see that the distribution

of the residuals with radius is basically the same with the largest residuals arising from the second and third outermost points. The innermost point contributes the next largest amount to χ^2 in that the emission is somewhat underproduced at this point. Now, the first issue that must be considered here is the manner in which we have treated the data for this instrument, which was discussed extensively in section III.(a) of TB. We noted that the data was divided into six azimuthal pie slices (Schreier et al. 1982) from which we picked one particular direction, which was determined to be relatively free of contamination from emission due to the jet or the radio halo, as representing the emission from the hot gas. (The data in each pie slice and the errors are listed in Table 1 of TB). Despite this choice, the count rate in other pie slices indicated that there were azimuthal variations in the count rate which we tried to account for by increasing the error bars associated with our data above the purely statistical values. (We could not account for these azimuthal variations in any case since we had assumed spherical symmetry). The question as to how well the HRI data are actually fit is therefore an uncertain issue. Certainly, in a qualitative sense, the total emission due to thermal processes in the inner regions of the cluster observed by the HRI has been well constrained. The quantitative nature of the fit, however, is still somewhat uncertain because of the inherent limitations of a spherically symmetric model. For example, in the analysis of Feigelson et al. (1987), at any given radius, the emission from the hot gas was taken to be from the azimuthal pie slice with the smallest number of counts. If we were to adopt this approach for the data, we see from Table 1 that the outer 3 points will not be decreased very much since our original choices were already rather low, but the four inner points will be considerably decreased. Under this circumstance, we see that the fit will be lowered at small radius to come into agreement with the lower values for the surface brightness. Therefore, the residuals from the second and third outermost points will then not be so significant. Other choices for the data could raise these two outer points. For example, if it is determined that the emission from the component morphologically similar to the radio halo is actually thermal in nature, then we must include this extra emission which we had previously discarded.

Yet other possibilities exist that may change the fit of our model to the HRI data. Since the background subtraction is performed by subtracting a constant level from the data, this could imply some correlation among the resulting data points, especially in the outermost points which have values that are not much larger than the background level

itself. The value of χ^2 would then suggest a worse fit than is actually the case. This is also a consideration which may apply to the IPC. Note that for this instrument additional errors were added to the statistical errors in order to account for background subtraction and vignetting uncertainties. Furthermore, the data were binned into 1′ rings, but the instrument point response was also on the order 1′. It is therefore uncertain if correlations could then have been introduced into the final data. Finally, in our fitting procedure, we have not considered the possibility of relative calibration differences for the instruments. For example possible systematic errors in the data of the FPCS could be as high as 30% (Canizares et al. 1982). A somewhat lower value for the FPCS lines could, for example lower the required emission in the region of the second and third outermost points in the HRI thus giving a somewhat better fit. We have tested for this possibility by making an additional fit to the data assuming that all of the measured FPCS line fluxes are reduced by 30%. The resulting fit is not improved relative to the fit assuming the originally measured values of the FPCS lines. In particular, the fit to the second and third outermost points of the HRI is not better with the reduced FPCS data. Also, the fit to the lines is somewhat worse than in the original case, and since the line fluxes have been reduced, the need for a cooling component to add emission to the lines at high temperatures is no longer required and the best fit value for the efficiency parameter q is very small, on the order of 10^{-6}. With the results of this test, we can conclude that the problem with second and third outermost points of the HRI is most likely an issue of only the HRI. This is additionally supported by the fact that in all of our models, including the single phase fits of TB, the predicted surface brightness profile at these outer points is consistently overpredicted.

We now summarize the results of the forging discussion. Because of problems with the data itself and the manner in which we have handled the data, it is difficult to accurately quantify the fit of our models to the data. In the case of the mass data, the inconsistency of two independent determinations makes the goodness of fit to one set of data difficult to judge. In the case of the HRI, the azimuthal variations of the HRI count rate and the proper assignment of the contributions due to various emission mechanisms makes it hard to chose the correct data for the fit. Additionally, the uncertainties of using a spherically symmetric model to understand data with azimuthal variations in the innermost regions of the cluster gas further renders the goodness of fit difficult to ascertain.

We now try to understand the effect on the single phase fit of including a cooling component. First, we see that the rather significant decrease in the contribution to χ^2 of the FPCS lines brought about by the inclusion of a cooling component arises out of a general decrease in the overall χ^2 in the multiphase case but offset by small increases in the contribution to χ^2 due to the other data. That is, while the contribution to χ^2 for the lines decreases by 12 for the 8 FPCS lines, the corresponding contribution for the HRI data, for example, increases by about 2.5 for 7 data points. The increase in the IPC part of the fit is about 4 for 26 data points and the increase from the mass part is about 1.5 for 7 data points. We conclude, therefore, that although the decrease in the total χ^2 for the fit is not large, the fit to the lines is significantly improved while, at the same time, the fit to the other data is not degraded by a considerable amount. The adoption of a cooling component therefore allows a simultaneous fit of the mass data and the FPCS line data that was not possible with only a single phase model. The increased emission at high temperatures due to the cooling component implies a higher predicted flux for the given lines thus solving the problem of the single phase fits. Again, this is exactly as expected from the qualitative considerations of TB. In summary, therefore, although the quantitative analysis of the fit to the data is complicated by the treatment of some of the data, we can conclude based on the significant decrease in the residuals in the FPCS part of the fit that the inclusion of a cooling component does indeed improve the fit in an important way.

We note before we proceed that an interesting question would be whether the addition of a cooling component will improve the fit when the constraints from the mass data are excluded. This would help us to better interpret the above result in that we can determine whether the mass constraints are the only data that are pushing for the adoption of a multiphase medium model. When such a fit is performed, we find that the best fit value for q, the cooling time efficiency, is 0. This indicates that indeed the mass data are the only constraints requiring a cooling component. In other words, a single phase model with all the low temperature emission coming from cool ambient gas provides a perfectly good explanation for all the X-ray data included in the fit. The data from the SSS is another matter which we will consider below. We can more explicitly understand this result by referring back to the temperature profile for the single phase fit to the data without mass constraints (the solid line of Figure 19 of TB). This temperature profile is perfectly satisfactory from the standpoint of the HRI, IPC, and FPCS data. However,

its steepness and its low value implies a mass profile that drops below the optical mass determinations. The mass data therefore provide the pressure to raise the temperature and to make it flatter. This then causes problems with the X-ray data (FPCS) unless the multiphase medium is considered. It is interesting to note that in the analytic solutions for an isobaric steady cooling flow of White & Sarazin (1987a), the temperature profile for the cooling time model are similarly flatter than the single phase solution.

We now come to the SSS spectrum. We first repeat briefly from section VI.(e) of TB for the sake of completeness the manner in which we have computed the results that are shown in Figure 9. First, we have used data from the same SSS observation as in TB. Our procedure has been to use the best fit cooling time multiphase model, whose density and temperature profiles are shown in Figures 3 and 4 as the solid line, to compute the predicted SSS spectrum. This is shown as the light solid histogram in Figure 9. Next, we have added a power law spectrum to this thermal component to account for emission from a central point source that was observed, for example by the HRI (Schreier et al. 1982), but not subtracted from the SSS data. The exponent of the power law is not well determined by the SSS spectrum but we have limited its value to the range from 0.4 to 1.0 in accordance with the methods of Lea et al. (1982). The normalization of the power law is determined by a χ^2 fit to the data. In addition, in this latter fitting procedure, we include a parameter which is the unknown absorbing column density of gas that will supposedly heavily obscure the central X-ray source. Finally, we have also included a parameter of the fit which determines the magnitude of the electronic background that is subtracted from the SSS data. As we discussed in TB, the SSS background consists of a component due to the particle background, and a component due to the electronics. The background due to the particles can be subtracted off immediately but only the shape of the electronic background is known. It's magnitude must be determined from a fit to the data, as we have done here.

In Figure 9, the data points with error bars are the fully background subtracted SSS data (including the subtraction of the electronic background) that are determined using the procedure outlined above. The heavy solid histogram gives the predicted SSS spectrum including the emission due to the power law component. Now, by comparing this figure to Figure 21 of TB, which shows the single phase fit to the SSS spectrum, we see that the the inclusion of a cooling component does not improve nor greatly change the fit. As in the

single phase model, the SSS spectrum at energies greater than about 1.4 keV is well fit, whereas the Fe L line complex at 1 keV and the oxygen line at 0.6 keV are poorly fit. Now, as was discussed in TB, White et al. (1991) deduced from SSS spectra that there was a need for both a cooling component to be added to the ambient intracluster medium in order to make up for the underprediction of the Fe L complex, and a column density of absorbing gas above the Galactic value in order to preferentially absorb out the excess emission at low energies. In TB, we first showed that adding extra absorbing gas to the model without a cooling component did not serve to improve matters in the low energy region. This was consistent with the findings of White et al. We have now shown, in Figure 9, that the case of adding only a cooling component without any extra column density likewise results in no improvement in the fit to the data. The fact that no improvement results from the inclusion of the cooling component can be easily understood. We will, however, delay a full discussion of this until we have presented additional fits which address the final possibility for improving the fit, namely the case where we include both the cooling component and the extra absorption.

We note, finally, that the predicted equivalent width for the 7 keV Fe complex for the above fit is 0.86 keV, which is slightly outside of the 1 σ error bar of the measurement. We have made an additional fit to the data with the same assumptions as the above multiphase fit but with a slightly higher assumed abundance for the elements other than oxygen. Here we take a value equal to 0.9 times solar instead of the 0.7 times solar value assumed above. In the new case, the best fit oxygen abundance is 3.7 and the best fit value for the efficiency parameter is $q = 1.1$. The quality of this fit is basically the same as the previous fit with 0.7 times solar abundance and the distribution of the residuals for all the data are basically the same. In addition, the the predicted SSS spectrum is also the same. For these reasons, we have not shown any of the results of this additional fit. It may be speculated, however, that an increase in the assumed iron abundance over the previous case should result in an increased emission in the Fe L complex part of the SSS spectrum, and, hence, an improved fit. But, as we will discuss below, the fact that the FPCS Fe L line complexes have to be fit in all cases implies that the the density and temperature profiles will be so adjusted in the new fit such that the total emission that comes out in the Fe L part of the SSS spectrum must be comparable from one case to the next.

b) Results with additional column density

In this section we present our results for the fit to the data assuming the cooling time model but with a value for the absorbing column density larger the Galactic value. We first assume the case where the additional absorption is distributed across the cluster such that the column density is constant with respect to the projected radius from the center of the cluster. Furthermore, we assume that the total column density is now $1.75 \times 10^{21} \mathrm{cm}^2$, which is the value as determined by White et al. (1991). The abundances of the metals other than oxygen are fixed at 0.7 times the solar value and the abundance of oxygen is allowed to vary.

The total χ^2 for this fit is 62 for 41 degrees of freedom and the best fit abundance of oxygen is 8.2 times solar. The best fit value for the efficiency factor q is 1.6. The above χ^2 now indicates a marginally acceptable fit (at about the 2σ level), which is an improvement on the fit with the Galactic value for the column density. (We will henceforth refer to this latter case as the "nominal case"). As we have done with the nominal case, to understand where the improvement comes from, in addition to plots of the density and temperature profiles, we have made figures that indicate the various contributions to χ^2. First, in figures 10 and 11, we show as the solid lines the density and temperature profiles, respectively, for the present case. (We will come back to this figure later to discuss the other lines, which correspond to fits with radially varying column densities, but we first concentrate on the solid lines). We can see that the situation that we have for the density and temperature profiles is very reminiscent of the single phase case examined in TB. Namely, the addition of extra absorption results in density and temperature profiles that are basically the same as in the case with only Galactic absorption. This is possible because the diminution of the emission in the model due to the extra absorption is made up by increasing the emission from oxygen. This, in turn, is done by increasing the relative abundance of oxygen with respect to the other metals to over a factor of 11 above the solar value. This property can, in fact, be seen in the subsequent figures.

For convenience, we now first describe the contents of the next few figures and then discuss them simultaneously. In figures 12 and 13, we have plot as the solid lines the predicted HRI and IPC surface brightness profiles, respectively. Again, the other lines corresponds to fits where the column density varies with radius and will be discussed later.

The FPCS residuals are given in panel (c) of Figure 14, and the predicted mass profile is given as the solid lines in Figure 15.

We see immediately from these figures that the major improvement in the degree of fit comes in the HRI part of the data where the contribution to χ^2 has been decreased to 8.1 from a value of 18.4 for the nominal case. The fit to the other data remains the same relative to the nominal case. Now, since the actual improvement comes in a sector of the data that does not have a statistically well defined contribution to χ^2, as described above, it is not possible to determined whether the overall decrease in χ^2 is really significant and, therefore, whether the new model constitutes an improved fit to the data. It is nevertheless clear how the increase in the column density has changed the fit. The increased absorption preferentially cuts down on the predicted emission as seen by the instruments at the lower energies. Therefore, in order for the Fe L lines and the OVIII Lyα line as seen by the FPCS to be simultaneously fit, the abundance of oxygen relative to iron must increase relative to the case with the lower column density to offset the increased absorption at low energies. Similarly, in both the IPC and HRI, in order to get the same total emissivities as in the case with the low column density, the decreased contribution from the lower energy parts of the spectrum must be offset by an increase in the oxygen abundance. Not surprisingly, these changes are exactly analogous to the changes brought about by an increased column density in the single phase case, as described in section IV.(d) of TB.

We can also recall that in the single phase models, the much increased oxygen to iron abundance ratio implied a decreased in the predicted equivalent width of the 7 keV iron complex. This then implied that in order to have agreement with the measured value of about 1 keV, we had to increase the absolute abundance of iron to over 2 times the solar value and the oxygen abundance to over 20 times the solar value. This rendered the fit unacceptable. We can ask whether the same situation arises in the current multiphase fit to the data. To check this we have computed the equivalent width of the 7 keV complex to be 0.6 keV which, as we expected, is too small relative to the observed value. By making additional fits with larger assumed values for the abundance of iron, we find that indeed we must again increase the abundance of iron to at least 2 times the solar value (and oxygen to at least 24 times the solar value) in order that the predicted equivalent width come to within 1 σ of the measured value. Therefore, this fit seems untenable in the same

manner as the single phase fit, namely, that the fit requires elemental abundances that do not appear to be reasonable (see TB, section IV.(d)).

For completeness, despite the fact that the current fit requires unreasonably high elemental abundances, we have computed the SSS spectrum to check the results of White et al. (1991) within the more general context of having included all of the available X-ray data. The predicted SSS spectrum for this case along with the data are shown in Figure 16. Again, the data are fully background subtracted and are represented as the data points with error bars. The predicted SSS spectrum from the thermal component alone is the light solid histogram and the predicted spectrum together with the added power law is the dark solid histogram. We can now draw the first conclusion. The inclusion of both extra absorption in the assumed manner (column density is constant with projected radius) and the assumption of the cooling time cooling flow model of White & Sarazin (1987a) does not provide an improved fit to the SSS data over that of the case with only Galactic absorption. We therefore conclude that if data from X-ray instruments other than the SSS are considered in conjunction with the SSS, the results of White et al. (1991) that extra absorption above the Galactic value is required to obtain an improved fit to the SSS data, are not confirmed. Furthermore, on comparing with the the fit of the case with just Galactic absorption in Figure 9, we see that not only is the fit not improved, the emission at about 0.65 keV is even somewhat higher in the present case than in the nominal case. Also, if we focus attention on the thermal component of the emission (the light histogram), we see that the emission that comes out in the Fe L complex relative to the magnesium line at about 1.5 keV is smaller in the case where a larger column density is assumed. A final property of the present fit is that the contribution from the power law component to the emission is much smaller than in the case where a lower column density was assumed.

The differences in the fit with extra absorption relative to the case with Galactic absorption as described above are not surprising since the same differences occurred in the single phase case. A complete analysis of the single phase case was given in TB, and since the current situation is very similar, we will only outline the reasons why the differences in the predicted SSS spectrum as detailed in the preceding paragraph exist. Section IV.(e) of TB can be referred to for the details. Now, the increased emission at around 0.65 keV in the SSS spectrum is due to the increased oxygen abundance required to fit the data with the presence of additional absorption. This arrises in the fit because of the FPCS data on

the Fe L lines and the OVIII Lyα line. Although the OVIII Lyα line is most decreased by the added absorption, the higher energy Fe L lines will still be somewhat effected. Since during the fit the abundance of oxygen is variable and the abundance of iron is not, the oxygen abundance is increased so that there is correspondingly more continuum emission due to oxygen in the energy range of the Fe L lines. This then allows the six FPCS Fe L line blends to fit although the resulting predicted OVIII Lyα flux is somewhat too large (see panel (c) of Figure 14; the FPCS residuals also change relative to the nominal case in the same way as the residuals for the single phase fits). This then implies that the 0.65 keV part of the SSS spectrum gets increased relative to the nominal case. The larger thermal emission at higher energies in the SSS (or the smaller emission due to the central power law component) can be understood in the same way as the increased emission at 0.65 keV. The larger continuum emission increases the contribution to the thermal emission at energies above the Fe L lines which accounts for the smaller amount of emission from the central power law source that is required to fit the data.

We argued qualitatively in the final section of TB that it is conceivable that the inclusion of a cooling component could effect an improvement in the fit of our models to the SSS spectrum. As we can see from above, this has not turned out to be the case. Furthermore, we showed in TB that in order to improve upon the fit to the SSS by including a cooling component, we had to first resolve an apparent inconsistency between the measurements of the FPCS and the SSS. As a reminder, this occurred for the following reason. The OVIII Lyα line and the Fe L line blends that are observed by the FPCS are well fit by our models. However, the SSS spectrum in the various energy ranges that correspond to these lines is not well fit by our predictions. Now, because it was demonstrated that at least half of the emission as seen by the FPCS in the single phase model came from within the SSS field of view, we have an inconsistency in that a fit to the data of one instrument does not automatically give a good fit to the other. In TB, we speculated that the assumption of a cooling component could solve this problem by moving the emission as seen by the FPCS to the region of the FPCS aperture that is outside of the SSS field of view by increasing the high temperature emission in the FPCS lines. Evidently, this has not occurred, which we can see by consulting Figure 17. Here we plot the flux of the eight observed FPCS lines as a function of temperature in the case where we have fit the data assuming Galactic absorption (the nominal case). Note that this plot is the cooling time

multiphase model analog of Figure 17 of TB where we showed the line fluxes in the single phase case. In Figure 17, the dark solid line corresponds to the OVIII Lyα line, the light solid line corresponds to the Fe XVII line and the other plots correspond to the various Fe L line blends. By referring back to the appropriate temperature profile (the solid line of Figure 4), we see that again, as in the single phase case, about half of the emission as seen by the FPCS comes from within the SSS field of view. We see that what has happened is that although the inclusion of the cooling component has moved the FPCS line emission to higher temperatures (compare Figure 17 of this paper to Figure 17 of TB) the temperature itself is raised in order to better fit the optical mass determinations. The net effect of these two changes is that the FPCS still samples mostly emission from the central regions of the cluster.

With the conclusions of the preceding paragraph, we can consider some of the questions that have been raised but are as yet unaddressed. We have already shown that the inclusion of a cooling component has improved the simultaneous fit of our model to the HRI, IPC, FPCS and the optically determined mass profile of Sargent et al. (1978). We can now understand rather easily why the inclusion of the cooling component does not improve the fit of the model to the SSS data in both the cases where the absorbing column density is assumed to be the Galactic value and where extra absorption is present. Because we know that the FPCS provides information on the same gas as the SSS, and because the OVIII Lyα line and some of the Fe L lines are observed by both instruments, the fit to the FPCS will determine the SSS flux at energies that correspond to these lines. Furthermore, it does not matter whether one has a single phase medium model, or a multiphase medium model, or even extra absorption. Any model that provides a good fit to the FPCS lines will automatically produce an SSS spectrum that has a fixed emission in the energy ranges of the observed FPCS lines regardless of the assumptions concerning the nature of the gas. Of, in the event that the SSS and the FPCS sample different parts of the gas, then our previous statements would not apply. However, it seems rather difficult, based on our conclusions, to arrive at a situation where this would be true. From a qualitative standpoint, the FPCS and the SSS have different apertures, but they are both strongly weighted towards emission in the central regions of the cluster. A situation where much of the emission from the cool lines as seen by the FPCS originates outside of the SSS field of view would imply that the cool gas resides outside of about 3' from the center of the

cluster and hotter gas sits in the center. This would seem to be an improbable situation from the standpoint of the SSS observations themselves. For example, it was determined by Lea et al. (1982) by fitting to the SSS spectra that a significant cool component exists within the SSS field of view. Also, Mushotzky & Szymkowiak (1988) arrived at a similar result based somewhat more sophisticated modelling of the SSS data.

We are now lead to the result that the measurements of the FPCS and the SSS do not seem to be consistent for a rather general set of conditions. The most serious discrepancy occurs in the energy range of the OVIII Lyα line where the FPCS requires about twice as much emission as the SSS. As explained in TB, the disparity in the results at 1 keV can be accounted for by problems with the atomic emissivity computations, however, this explanation cannot resolve the problem at 0.65 keV. It is also not possible for us to determine exactly why the inconsistency in the OVIII Lyα part of the spectrum occurs from our present analysis. However, several possibilities do present themselves. First, the problem could be with the relative calibration of the FPCS and the SSS. Both of these instruments were calibrated to the Crab. However, this procedure requires some modelling of the remnant (Schattenburg et al. 1980 and Schattenburg et al. 1986) which could therefore affect the relative normalizations of the count rates from the two instruments. Uncertainties in this procedure are supposedly accounted for in the systematic uncertainties associated with each instrument. In the case of the FPCS, the quoted level of systematic uncertainties is on the order of 30% (Canizares et al. 1982) which is too small to account for our inconsistency. Another possibility is that there may yet be problems with the detailed ice model that was used in order to correct the response matrix for the buildup of ice during the course of the observations. Again, we have no means to explore this possibility but only point it out as a possibility.

Finally, to access the magnitude of the discrepancy at low energies and to see if the SSS is also discrepant with respect to the HRI which is the other instrument that views the central regions of the cluster, we have made an additional fit to the data excluding data from the FPCS (i.e. we have used data from the HRI, IPC, and the optically determined mass profile). We have furthermore fixed the abundances of all metals to be half solar and the column density of absorbing gas to be the Galactic value. We have done this with the following in mind. The large amount of emission in OVIII Lyα seen by the FPCS is the element which drives up the abundance of oxygen relative to the other metals and which

also drives up the emission at 0.65 keV in the predicted SSS spectrum. By holding the abundance of oxygen down to the same level as the other elements and by removing the agent that pushes for the higher oxygen abundance, we can assess whether we would still have as significant a problem with the overprediction at 0.65 keV as before. In Figure 18 we show the predicted SSS spectrum for this fit (light solid histogram) along with the data. On comparing with Figure 9, which gives the corresponding fit to the SSS which includes data from the FPCS, we see that for the most part, the fit at energies larger than about 2 keV are equally good in both cases. The lower energy magnesium line at around 1.5 keV is, however, somewhat worse fit in the case where we have left out information from the FPCS. This is not surprising in that the spectral characteristics of the lower temperature gas has not been specified because the FPCS data have been left out. Furthermore, the SSS spectrum at energies lower than this will not necessarily give the same degree of fit as in the case where FPCS data are included. Now, the point here is that although the predicted emission at around 0.65 keV has been cut down considerably relative to the case where FPCS data have been included, there is still some excess in the predictions at low energies relative to the data. We can therefore conclude that even without the FPCS, when Galactic absorption is assumed, the remaining HRI data still requires that there be some degree of emission above the SSS limits at low energies even when the relative abundance of oxygen to iron is held at the solar value. We note that there is somewhat more emission in the Fe L lines and the 1.5 keV magnesium line because, in order for the HRI data to be fit, the decrease in the emission at low energies much be made up by an increase in the emission at higher energies. We note further that, consistent with the decrease in the low energy emission in the SSS, the predicted FPCS OVIII Lyα line flux (which is not included in the fit) is lower then the observed value by about a factor of 6 and the flux of the other low temperature lines (e.g. FeXVII) are also reduced.

We can now ask what manner of absorption is required to further reduce the emission at low energies so that we finally get agreement with the low energy part of the SSS data. The dark solid histogram in Figure 18 shows the predicted SSS spectrum when we refit our model to the data, again excluding FPCS data, with a higher absorption. We have again assumed that the abundance of all the elements is half the solar value, but this time we have assumed that the total column density is $1.75 \times 10^{21} \mathrm{cm}^2$. We see that we now have very good agreement at the lowest energies and up to about 1.1 keV where the predicted

SSS spectrum then goes far above the data. That this happens is easy to understand. The significantly decreased emission at low energies again requires the emission at high energy to be enhanced so that the HRI data can be well fit. The reason that the emission at higher energies is so much overproduced in this case is that the HRI effective area is higher at the lower energies of the OVIII Lyα line. Therefore, to make up for the lost emission at low energies by increasing the emission at high energies, the amount of high energy emission that is added must be more than the amount of low energy emission lost. Furthermore, the HRI effective area drops off rather significantly above an energy of about 2 keV so emission above that energy hardly contributes at all to the HRI count rate. Note further that there is no reason that the line features should be well fit in this case because there are no constraints on the spectra once the FPCS data have been excluded. In fact, the predicted flux in the FPCS OVIII Lyα line is now even lower than in the above case with Galactic absorption, again consistent with the lower emission in the SSS at low energies.

We now summarize the conclusions from the two test cases presented above. First, we had previously concluded that the measurements of the FPCS and the SSS were discrepant in the low energy regime around 0.65 keV as well as in the Fe L region of the spectrum, although this latter problem could conceivably be fixed by readjustments in the atomic emissivities. We have now learned that the HRI is also inconsistent with the SSS for the following reasons. First, if we assume Galactic absorption, we find that a fit to the data excluding FPCS data still implies some degree of overprediction at low energies and a poor fit to the Fe L lines. When we further try to fix the low energy part of the fit by adding extra absorption, we then find that a good fit to the low energy part implies a vast overprediction at higher energies in the SSS. This is required in order to produce enough emission as seen by the HRI to fit the data. We emphasize that these results hold despite the fact that we have excluded the possibility of an overabundance of oxygen and the effects of a strong OVIII Lyα line as measured by the FPCS.

We now consider the case where the additional column density varies with radius as evaluated by using eq. (10). As we stated in section II, the observational justification for considering this case stems from the disparate determinations of the column density from various sources. Spectral work from the IPC (Fabricant et al 1980; Fabricant and Gorenstein 1983) indicate that the column density in the outer regions away from M87 is consistent with the Galactic value. On the other hand, work on data from the SSS

(Lea et al. 1982, White et al. 1991) have always indicated a higher value for the column density. Since the SSS observations were taken of the central regions of M87, the two disparate values could be consistent if the column density were taken to be radially varying with a higher value in the center of the cluster and the lower Galactic value further out from the center. As an initial demonstration that our approach of using eq. (10) is at least reasonable, we first take our best fit model assuming a Galactic column density and compute the additional column density that would have accumulated over the lifetime of the cluster. Note that this is not a self consistent calculation; the additional column density that results from the gas dropping out of the ambient phase has not been taken into account in the computation of the emission from the model. We are simply showing that the column density that would have arisen has values which can reasonably have the desired effects on the fit. In figure 19, we show the additional column density, N_{extra}, as a function of projected radius for this case as the dark solid line. Note that in making this plot we have assumed that the lifetime of the cluster t_{max} is 10^{10} years and that the fraction of the condensing material that becomes absorbing gas is unity. Also note that since the density of absorbing gas responsible for the extra absorption ρ_c varies with radius, the column density will change depending upon where along the line of sight we are considering. For the purposes of this figure, the column densities plotted here are for a line of sight that goes half way through the cluster gas. That is, the total extra column density through the cluster is just two times what we have plotted in this figure.

Now, the light solid horizontal line indicates the value of the Galactic column density of $2.5 \times 10^{20} cm^2$. We see that outside of the SSS field of view of 3', the extra column density is below about 20% of the Galactic value and hence does not contribute significantly to the total absorption. Inside of this radius, however, the extra column density rises to a value comparable to the Galactic value at a radius of about 0.6'. We see, therefore, that indeed we have the possibility of reconciling the higher column density as determined by the SSS and the lower, Galactic column density as determined by the IPC. The other plots of the figure refer to results of self consistent computations which will described below.

We now go back to Figures 10 through 15 where we show the results of self consistent fits to the data using eq. (10) to compute the additional column density. The results are shown for three of our fits to the data corresponding to three different assumed values of t_{max}, namely 10^{10} years, 5×10^{10} years, and 10^9 years. Why we have chosen these

particular values will be made clear below. We note that as with our other fits, we have again specified that the abundance of metals other than oxygen is fixed at 0.7 times solar and we have allowed the abundance of oxygen to vary. We now first discuss the quality of the fits to the data. In Figures 10 and 11 we show the density and temperature profiles that result from our fits. Recall that the solid lines gave the profiles in the case where the additional column density was uniformed distributed across the cluster. The dotted line gives the results when t_{max} is assumed to be 10^9 years, the short dashed line corresponds to the case of 5×10^{10} years and the long dashed line gives the case where t_{max} is 10^{10} years. We see that in the cases where the extra absorption varies with radius, the density profiles are slightly higher at all radii relative to the model with uniform extra absorption. We would initially expect, however, that the opposite result should hold. That is, since in the radially varying case the total column density is almost the Galactic value at large radius, we have less absorption relative to the case with uniform absorption and hence a need for less predicted emission from the model. This, in turn implies a smaller density. The reason that this expectation is not met is that the oxygen abundance has been allowed to vary in the fits and the best fit oxygen abundance in the case with uniformly higher absorption is so high (8.2 times solar) and contributes so much emission that a lower density is required despite the higher absorption. As for the temperature profiles, we see that the profiles are essentially the same in all three cases with radially varying absorption. Additionally, the profiles are essentially the same as that of the case with the uniformly higher absorption and the case with Galactic absorption. Taken together, this information indicates that regardless of the assumptions concerning the absorption, given that the multiphase model is the cooling time model, the temperature profiles are rather well determined and are very close to power laws in the region where data exists.

Now, in Figures 12 through 15, we display the fit of our model to the data. The total χ^2 in all three cases is about 79 for 41 degrees of freedom. This would naively indicate about as good a fit as the case with the assumption of Galactic absorption. As before, we now look at the various contributions to χ^2 to further assess the goodness of fit in these cases. The predicted HRI and IPC surface brightness profiles are shown in Figures 12 and 13, respectively, with line type assignments that correspond to those of Figures 10 and 11. (The predicted IPC surface brightness profiles are so similar that the lines overlie each other). The FPCS line residuals are shown in Figure 14 with the same conventions

as for previous cases. Here, panel (d) gives the case where t_{max} is 10^{10} years, panel (e) corresponds to 5×10^9 years, and panel (f) corresponds to 10^9 years. Finally, the mass profiles are shown in Figure 15. The predicted profiles are again so similar that they lie on top of each other along the light solid line. By comparing the predictions in the cases with radially varying column density with the predictions of the case with Galactic absorption, we see that in all cases the contribution to χ^2 from the various parts of the data are comparable. For example, in the case of the FPCS, by comparing panels (d),(e) and (f) of Figure 14 with (b) of Figure 7 (which gives the case assuming Galactic absorption), we see both that the residuals are distributed in the same manner in both cases and that the total contribution to χ^2 in both cases are basically the same. In a similar manner, the contribution to χ^2 from the other parts of the data can be compared. The conclusion then is that including absorption due to gas cooling out of the flow assuming that all of the condensing gas goes into absorbing X-ray emission does not change either the character or the quality of the fit to the data relative to the case where only Galactic absorption is assumed. Furthermore, this conclusion also holds for other values of t_{max} not shown here since even the case which gives the largest plausible absorption, namely the case where t_{max} is 10^{10} years, indicates no change in the fit. If t_{max} is taken to be some smaller value, a lesser amount of gas would have had a chance to condense out of the flow and, hence, will have had a smaller effect on the fit to the data. In a similar manner, if only a fraction of the cooling material were to go into absorbing gas, again, there would be less column density than in the case where all of condensing gas absorbs the emission and t_{max} is taken to be 10^{10}. The effect on the fit would therefore be correspondingly less than in the "maximal" case.

We now try to understand why the fit is unchanged with the inclusion of the extra absorption. For this purpose we refer back to figure 19. Recall that here we plot the total extra column density half of the way through the cluster along a line of sight with a given projected radius. The long dashed line gives the column density that corresponds to the case where t_{max} was assumed to be 10^{10} year, the short dashed line gives the case of 5×10^{10} years, and the dotted line corresponds to the case with the shortest t_{max} of 10^9 years. We note first the reasonable property that the shorter the assumed lifetime of the cluster, the smaller the additional extra column density. We can now understand why the fit is not changed by including extra absorption. For most radii, the column density

is much smaller than the Galactic value. Only at the innermost regions is it comparable to the Galactic value. We can now understand the effect of this extra absorption on the model predictions for each instrument. First, since the IPC looks at the part of the data outside of about 3', it will not be effected. As for the FPCS, about half of its emission in the various lines comes out at radii outside of 3' and the other half comes from inside of this radius (see Figure 17). In addition, the Fe lines arise at energies of around 1 keV which will not be that greatly effected by the extra absorption. We can therefore conclude that the predicted flux from the Fe lines of the FPCS will also not be greatly effected. The OVIII Lyα line on the other hand occurs at a lower energy and will be more significantly effected. However, again, only a minority of the emission comes out at radii where the additional column density is significant. Therefore, although the OVIII Lyα line flux will be effected more than that of the Fe lines, still, there will be little real effect of the extra absorption on the line flux. The surface brightness predictions for the HRI, however, especially at the innermost points of 10" and 25.1", will be significantly effected by extra absorption, reducing the predicted emission by a large fraction. We can then ask how the fit to the data can be fixed so that the aforementioned problems with the HRI can be resolved and the fit improved. Since the HRI is most sensitive to low energy emission, namely emission at around the energy of the OVIII Lyα line, the emission can be increased by increasing the abundance of oxygen. This will in fact also serve to increase the predicted flux of the FPCS OVIII Lyα line which, as stated above, has been somewhat effected by the extra absorption. In fact, the best fit abundance of oxygen for the case with t_{max} of 10^{10} years is 3.3 times solar, the best fit value for the case where t_{max} is 5×10^9 years is 3.2 times solar, and the value in the case of t_{max} equaling 10^9 is 3.1 times solar. These values compare with 2.7 times solar in the case where only Galactic absorption is assumed.

We come to the issue of why we chose to show the three specific cases of Figure 19. First, the case where t_{max} is 10^{10} years represents something of a maximum value (up to a factor of about 2) for the cluster lifetime. We can then ask what is the value of R_{max} as determined from eq. (11) corresponding to some representative radius where ρ_c is to be determined. The point here is that this will enable us to determine if the model is plausible from the standpoint that the maximum radius lies within the bounds of the part of the cluster that we have modelled. Since our modelling has only been done for gas that is relatively close to the center of M87, if R_{max} is rather large, and if the contribution to

the integral that gives ρ_c (eq. (10)) is large from these outer radii, then we may not have a very physically plausible situation where a significant part of the cooled gas actually comes from outside of the cluster itself or from outside of the part of the cluster that we have modelled. To check this we first find that in the case where t_{max} is 10^{10} years, for an inner radius r of 1 kpc, the corresponding R_{max} is about 8 Mpc. This is clearly way outside of the bounds of the cluster and represents a situation that is not very physically realistic. The case where t_{max} is 5×10^9 years gives a R_{max} of about 4 Mpc, which is again rather unreasonable, but the case where t_{max} is 10^9 year gives a R_{max} of about 670 kpc (about 150' for our assumed distance to M87) which is well within the the cluster limits and only somewhat outside of our modelling region. Now, in a realistic situation, the cluster lifetime could indeed be as long as 10^{10} years but the extent of the gas would be limited beyond a certain radius whereas the gas in our model goes out to infinity. Therefore, in a realistic situation, R_{max} would be limited by the extent of the cluster regardless of the cluster lifetime. We can therefore regard our present model fit with an assumed cluster lifetime of 10^{10} years as giving an upper bound on the amount of condensed gas that could have come out of the flow. A more realistic scenario for this case would then be rather close to just a fit with a smaller value for t_{max} (hence smaller value for R_{max}) even though the actual cluster lifetime is longer. On the other hand, should the cluster lifetime indeed be shorter than 10^{10} years, the case where the lifetime is assumed to be 10^9 years gives a realistic view of the situation with an R_{max} that lies comfortably within the reasonable bounds of the cluster. Should the lifetime be even shorter, the fit will not change much from this aforementioned case since the properties of the fit with the extra absorption is already basically indistinguishable from the fit which assumes only Galactic absorption. We can conclude then that since the range of cases that we have presented basically bounds the physically realistic regime for different assumed cluster lifetimes, and since the properties of the fits in all of these cases are similar, the fits that we have presented provide a realistic picture of the fit with the actual cluster lifetime (whatever that happens to be) and the actual extent of the cluster gas.

We finally turn to the predicted SSS spectrum. We have not shown our spectrum here since it is again basically the same as that pictured in Figure 9. The previously considered problems with the overprediction at 0.65 keV and underprediction at around 1 keV persist even in our present fits. This is understandable from the standpoint of our discussion

above. Namely, since around half of the emission as seen by FPCS comes from within the SSS field of view, the data on the FPCS OVIII Lyα line flux still places constraints on the predicted SSS emission at around 0.65 keV. The inclusion of a self consistently determined profile of extra absorption does not help solve the disparity between the FPCS measurements and the SSS measurements.

IV. RESULTS FOR POWER LAW MODELS

a) Results with a Galactic column density

In this section we present the results of a multiphase analysis of the data assuming that the rate at which gas drops out of the ambient medium is given by eq. (7) and that the emissivities are given by eq. (8). The parameter N_{mult} is treated as a parameter of the optimisation process but the parameter α_{mult} will be held fixed for each given fit. A range of values for α_{mult} are considered and we present here the case which gives the best fit to the data. We again assume that the abundance of metals other than oxygen is held fixed at 0.7 times the solar value and we also assume for this section that the column density is the Galactic value.

The first result that we find from our power law fits is that the preferred value of α_{mult} is 3.5. Actually, α_{mult} is not that well constrained but values between 3 and 4 giving a total χ^2 that is very close to the best fit case. Outside of this range of values for α_{mult}, the total χ^2 is considerably larger. The foregoing conclusion contrasts with the often quoted result that the total mass accretion rate within a radius r goes like $\dot{M}(r) \sim r$ which corresponds to $\alpha_{mult} = 2$. With our best fit case, it is not meaningful to compute the total mass accretion rate within a radius r for our best fit $\dot{\rho}$ since it is everywhere divergent. Of, this is not the case in reality since our form for $\dot{\rho}$ will certainly not be valid all the way into the center of the cluster. At some point, it will flatten out but since we have not modelled the most central regions we cannot determine the form of $\dot{\rho}$ there. (We will, however, try a fit with a flattened power law to assess possible improvements in the fit; see below).

In Figures 20 and 21, we plot as the solid line the density and temperature profiles that result from our fit to the data assuming $\alpha_{mult} = 3.5$. The dotted lines in these figures and the subsequent two figures correspond to a fit assuming extra absorption which we will

discuss later. The total χ^2 of the present fit is 71 for 41 degrees of freedom (7 HRI points, 26 IPC points, 8 FPCS lines, 7 mass points, minus 7 parameters, 5 associated with the density and temperature profiles, the variable abundance of oxygen, and $N_{\rm malt}$ associated with the cooling component). Also, the best fit value for the oxygen abundance is 6 times the solar value. This value for χ^2 would initially seem to imply that the fit to the data is rather poor but slightly better than the fit with the cooling time model. We will show later, however, that the fit to the data is less satisfactory than in the cooling time model. We first briefly consider the density and temperatures distributions. On comparing our profiles here to the corresponding profiles in the case of the cooling time model, we see that in general, they are similar in form but that the temperature in the present case is slightly higher at small radius. This is simply a refection of the fact that the power law profile for $\hat{\rho}$ is more steeply peaked at small radius than the cooling time model and will imply somewhat more emission from the cooling component. The temperature then need not be as low as in the cooling model case in order to produce sufficient emission to fit the data.

As in the case of the cooling time models, we will now display the various contributions to χ^2 in order to assess the effects of including a power law cooling component. The predicted HRI and IPC surface brightness profiles are shown as the solid lines in Figures 22 and 23, respectively along with the data (points with error bars) and the FPCS residuals are plotted in panel (g) of Figure 24 in the same manner as Figures 7 and 14. We have not shown the predicted mass profiles since they are basically identical to the predicted profiles in the cooling time models shown in Figure 15. We can now first analyse these figures in the same manner as in the section III. First, as to the goodness of fit we are again plagued by the problems of not knowing exactly how to correctly treat the data in the case of the HRI and the optical mass determinations. In the mass part of the fit, we have the problem with the inconsistency of the two outermost data points, which are from the determinations of Sargent et al. (1978), and the mass as derived by Mould et al. (1987). In our present fit, we have a contribution to χ^2 due to the mass part of the fit of 18.6 which is comparable to the case where we assumed a cooling time model. Furthermore, we again have the situation where the largest residuals comes from the two outermost points. Therefore, because of the problems with the outermost mass points, it is not clear for our

present fit with a power law for the mass dropout rate whether the large contribution to χ^2 indeed implies a poor fit to the data.

In the case of the HRI part of the fit, however, the situation is rather different than in the cooling time model. The contribution to χ^2 in the present case is 8.7 for 7 data points which now indicates a rather good fit as compared to a χ^2 of 18 in the case of the cooling time model. This would indicate that the fit to HRI part is much better in this case but, again, we must be cautious. As stated above, the χ^2 from the HRI part of the fit cannot be considered to give precise statistical information on the goodness of fit because of uncertainties in the way that the data is treated. Now, in the same way that we could not conclude that the large contribution to χ^2 in the case of the cooling time model necessarily indicated a poor fit to the data, we cannot conclude here that the much lower χ^2 in the case of the power law model indicates a good fit. In fact, if we again compare the fit to the HRI data in this case to the fit of the cooling time model (solid line of Figure 5) we see that the major change has been that the predicted surface brightness is more steeply peaked in the center with the power model than in the cooling time model. This is again brought about because $\hat{\rho}$ is more steeply peaked in the central regions than in the cooling time model therefore implying more emission from the central regions (see Figure 25 below). This fact also allows an improved fit at the second and third outermost points because the cooling component gives emission that is centrally peaked enough that the emission in the outer points is lower. Now, as we have discussed previously, it is not clear whether the high central emission that is indicated by our choice of the data is really indicative of the distribution of the gas. Some other choice for the data from a different azimuthal pie slice (see Table 1 of TB) for the innermost radius can result in a lower value for the central emission. The corresponding increase in the central emission by including a power law model cooling component will then, in fact, worsen the fit. In conclusion, therefore, it is not clear based on uncertainties associated with the data whether the reasonable contribution to χ^2 from the HRI data in fact indicates a good fit. It can be concluded, however, that the total emission in the central regions have been well constrained in at least a qualitative sense and is the same manner of conclusion that was dawn in the case of the cooling time model.

The IPC part of the fit gives a contribution to χ^2 of 26 for 26 data points which indicates a rather good fit. As in our discussion of the cooling time model, this does

indeed represent a relatively good fit since the issues that made the HRI data difficult to handle are not very important in this case. This point has been discussed more fully above and in section III.(b) of TB. Finally, we move on to the FPCS part of the fit. From panel (g) of Figure 24, we see immediately that the FPCS residuals are large and the fit to the data very poor. A comparison with the single phase fit in panel (a) of Figure 7 indicates that the fit to the lines is only insignificantly improved with the inclusion of the cooling component. This contrasts sharply with what happened when the cooling time model was adopted where the FPCS residuals were decreased so that the fit to the lines then became rather good. These results can be easily understood. Because the power law rises relatively slowly at large radius and then becomes very peaked near the central regions, there is not much emission from this component except at very small radii. This fact is reflected in the strong central peak in the predicted HRI spectrum inside of about 50″ or so. However, the fact that there is not much emission from this component further out in the cluster implies that there is not that much contribution to the emission as seen by the FPCS. Again, this is true since the emission as seen by the FPCS is broadly distributed over radius (see Figure 17). From our previous arguments, in order to improve the fit of our single phase models to the data in light of the higher central temperatures required by the mass data, we had to somehow increase the higher temperature emission in the FPCS lines so that the FPCS data could then be fit. In the present case, there is not much of the higher temperature emission produced by the cooling component so the fit to the FPCS data is not improved. To show this graphically, in Figure 25, we have plotted $\dot{\rho}$ as a function of radius that results from our various fits. The solid line corresponds to the best fit cooling time model with galactic absorption, the dotted line corresponds to the present best fit power law model, and the short dashed line corresponds to a flattened power law which will be described later. We can see quite readily the property that we have discussed above that in the region where the emission as seen by the FPCS arises, the contribution from a cooling time model is much more significant than from a power law model. We can therefore conclude that the addition of the power law cooling models do not provide an improvement to the fit to the data in a meaningful way and that a pure power law in radius does not offer a good description of $\dot{\rho}$.

We have not shown the predicted SSS spectrum in this case since it looks similar to the previous SSS fits with the cooling time model. Again, the fit at energies larger

than about 1.2 is good, but the model significantly overpredicts the emission at 0.65 keV and underpredicts the emission at 1 keV. This is again understandable for the following reasons. First, for the the energy range around 0.65 keV, although all the FPCS lines are not well fit, the OVIII Lyα line in particular is well fit (see panel (g) of Figure 24). It therefore again forces the predicted emission at 0.65 keV in the SSS spectrum to be the same as in the fit with the cooling time model (Figure 9). As for the Fe L line blend, although the residuals from the subset of lines observed by the FPCS is rather large, we can see from panel (g) of Figure 24 that the residuals are distributed such that some of the lines are underproduced and some are overproduced. Not surprisingly, then, the total Fe L emission as seen by the SSS at 1 keV has been constrained to be at the same level as in a case where the lines are well fit.

In conclusion, we have found that when we include a cooling component where the dropout rate from the ambient intracluster medium, $\dot{\rho}$, is given by eq. (7), the fit to the data relative to the single phase case is not improved in a meaningful way. Namely, although the total χ^2 in this case is smaller than that of the single phase fit, the reduction in χ^2 came primarily from the fit to the imaging data. The residuals in the fit to the FPCS lines in the single phase case, which are unreasonably large because of the higher temperatures required to fit the mass data, are not reduced by the inclusion of a power law cooling component. Since our goal was to improve the FPCS part of fit, the inclusion of the cooling component of the assumed form has not improved the fit and is not preferred over the cooling time multiphase model.

b) Results with additional absorption

We now consider the fit to the data assuming a power law form for $\dot{\rho}$ but with extra absorption. For these fits, we have again specified that the column density of absorbing gas is uniform across the cluster with the value as determined by White et al. (1991) of $1.75 \times 10^{21}\mathrm{cm}^2$. We assume that the abundance of metals other than oxygen is 0.7 times the solar value and that the abundance of oxygen is variable. We find that the best fit value for α_{mult} is 3.0 in this case, although, again, values of α_{mult} between 3 and 4 give total χ^2 that are basically the same. The total χ^2 in the best fit case is 62 for 41 degrees of freedom and the best fit abundance of oxygen is 22 times the solar value. Again, as in the single phase models and the cooling time models, an increase in the absorption has

resulted in a decrease in the total χ^2 as well as an increase in the abundance of oxygen. The indicated value of χ^2 would now seem to imply a somewhat reasonable fit (2σ) but as before, problems with this fit as well the question of parts of the fit are improved indicate that no real improvement is obtained.

The density and temperature profiles are given as the dotted lines in Figures 20 and 21. We see that there is not much difference between the profiles for this case as compared with the case with Galactic absorption. Again, the increased absorption has been offset by the strongly increased abundance of oxygen. The one difference, however, is that density profile is somewhat steeper at small radius than the case with Galactic absorption. This is just because in the present fit, the preferred value for $\alpha_{\rm mult}$ is 3.0 instead of 3.5 which is the value in the case with Galactic absorption. This means that $\dot{\rho}$ is less steep at small radius in this case and that the there will be less emission at small radius due to the cooling component. This then implies that the density must be somewhat larger at small radius in order to give the right amount of total emission at small radius.

As for our previous cases, we try to understand the various contributions to χ^2 by plotting out the respective contributions from the various parts of the data. The fit to the HRI is shown as the dotted line in Figure 22, the fit to the IPC is shown as the dotted line in Figure 23, and the residuals from the FPCS lines are shown as panel (h) of Figure 24. We can see that for the two imaging instruments, the fit is somewhat improved relative to the case with Galactic absorption. For the HRI, we get a contribution to χ^2 of 3.6 (as opposed to 8.6) for 7 data points and in the case of the IPC, we get a contribution to χ^2 of 20.6 (as opposed to 26.6) for 26 data points. This is reminiscent of the improvement brought about by extra absorption in the single phase models and in the case of the cooling time model fit in that the improvement comes from the fit to the imaging data. Now, like these previous models, the improvements in the fit to the imaging data may not represent any actual statistically meaningful improvements. Recall that for the HRI, because of the nature of the data (large azimuthal variations) and the error bars (additional systematic errors), there was some uncertainty as to the correct way to treat the data itself. In the case of the IPC, we can presume that the improvement could be due to the unreasonable abundances of the elements. This is because the predicted 7 keV equivalent width for this case is 0.45 keV which is too low relative to the measured value of 1 keV. By making additional fits with higher abundances of the metals other than oxygen in order to increase

the predicted 7 keV equivalent width, we find, as in the previous cases, that an abundance of more than 2 times solar is required. Additionally, the required abundance of oxygen is more than 40 times the solar value. This then makes the fit unrealistic because of the unreasonable required abundances.

From panel (h) of Figure 24, we see that the fit to the FPCS data is not improved relative to the case with Galactic absorption. We did not expect any improvements because the increased absorption will not serve to increase the high temperature emission in the FPCS lines. We note further that the flux of the OVIII Lyα line is increased relative to the case with Galactic absorption in exactly the same manner and for the same reason as in the single phase models and the cooling time model fit. In addition, the SSS spectrum, which we have not shown, is very similar to previous cases exhibiting a good fit for energies greater than about 1.2 keV, underprediction of the Fe L complex and overprediction of the OVIII Lyα region of the spectrum.

We conclude from this section that in the case where assumed that $\dot{\rho}$ is given by a pure power law, there is no evidence that an increased column density of absorbing gas will give an improved fit to either the SSS data or data from the other *Einstein* instruments. Furthermore, by assuming additional absorption, we required unreasonable abundances of the metals in order to fit the data thus implying that extra absorption is not indicated.

b) Results with a flattened power law

In light of the poor fit of the power law models to the FPCS line data as shown above, we can ask whether any simple modification of the model may result in a better fit to the data. We noted that the reason that the power law model provided a poor fit was that the steepness of the profile at small radius implied very little emission outside of the central regions. We can therefore attempt to extend the emission to the outer regions and soften the emission in the inner regions by allowing for a core radius. With this notion, we have made additional fits assuming the form

$$\dot{\rho} = N_{\rm mult} \left[1 + (\frac{r}{a_{\rm mult}})^2\right]^{-\alpha_{\rm mult}} \qquad (13)$$

where now we have an additional parameter $a_{\rm mult}$ which is the core radius for the density accretion rate. Note that the form above gives a power law at large radius and flattens to

a constant value at small radius. Now, in the fitting process, as before, we vary $N_{\rm mult}$ and $a_{\rm mult}$ along with the other parameters of the fit but we fix $\alpha_{\rm mult}$ for a given optimization. We then take another value for $\alpha_{\rm mult}$ and we perform another fit to the data. This process is repeated for a variety of values for $\alpha_{\rm mult}$.

In this way, we have found that the best value for $\alpha_{\rm mult}$ is 1.75 (which corresponds exactly to the case of $\alpha_{\rm mult} = 3.5$ in eq. (7)) although again a small range of values around $\alpha_{\rm mult} = 1.75$ gives total χ^2 that are relatively close to that of the best fit case. This total χ^2 is 74 for 40 degrees of freedom with a best fit oxygen abundance that is 5.8 times solar (again, the other metal abundances are fixed at 0.7 times solar), and the best fit value for $a_{\rm mult}$ is 0.82 kpc. Now, the quoted value for χ^2 is basically the same as for the best fit with a pure power law model and it also turns out that the distribution of residuals in the current fit is also basically the same. Because of this latter property, we have not shown the results of the present model but we do try to understand these results. To this end, we show in Figure 25 $\dot{\rho}$ as a function of radius that results from our best fit case assuming the form for $\dot{\rho}$ of eq. (13). We see that, as we expect, outside of a radius of about 0.4', we get a power law with the same slope as the best fit case of the pure power law models. The offset in the two cases is due to a somewhat different distribution of emission between the ambient phase and the cooling phase. That is, in the case where we have a pure power law, we have slightly more of the emission coming out from the ambient phase relative to the case with the flattened power law. The reason for this offset will be clear momentarily, but first we focus on Figure 25. Now, since the core radius for $\dot{\rho}$ is small, for most regions where we have constraints from the data we again basically have a power law model. For example, in the case of the IPC, the innermost point that we use is at 3.5' where we clearly are in the power law regime. For the FPCS, by consulting Figure 17 for instance, we have a similar situation. In fact, since the power law drops off so fast at large radius, there is little emission coming from the cooling component at these radii relative to the emission from the ambient phase. We therefore have two conclusions. First, since most of the emission coming out in the regions viewed by the instruments that we are considering is only from the ambient phase, the fit to these instruments should have the same properties in both the flattened power law model and the pure power law model. This is exhibited as the similarity of the residuals in the fits assuming the two cases. The second conclusion is that since at most radii the majority of the emission is

from the ambient phase anyway, a slightly larger $\dot{\rho}$ in the case of the flattened power law will not result in any extra emission above the case with the power law model. Now, as for the reason why $\dot{\rho}$ for the flattened power law ends up higher than in the case of the pure power law, we must look at the innermost points of the HRI where there is a significant contribution of the cooling component to the emission. As a reminder, the innermost HRI point that we will consider is at 10". Now, at these radii, in order that the HRI data be fit, the emission from the cooling component must be comparable in the two cases, hence the value for $\dot{\rho}$ must be comparable. In Figure 25, we see that the curves giving $\dot{\rho}$ cross basically at the innermost radius where HRI data are used. This then determines the normalization of the flattened power law relative to the pure power law.

We expect that the power law form for $\dot{\rho}$ will certainly not extend all the way to the center of the cluster, otherwise we would get infinite emission at the center and an infinite value for the mass accreted inside of a given radius r. The flattened power law fits of this section then offer us a somewhat more physical accretion law in the sense that at very small radius, $\dot{\rho}$ flattens out but in the region that is viewed by the instruments, the same results are obtained as in the power law case. We will therefore use the form of $\dot{\rho}$ in eq. (13) for our subsequent computation of the total accretion rate within a given radius r. Note however, that despite the improved properties at the center, a flattened power law form for $\dot{\rho}$ still does not provide an improvement in the fit to the FPCS lines over the single phase case.

V. MASS ACCRETION PROFILES

In Figure 26 we show the mass accretion profiles for the various cases that we have considered. The plots give the total mass accreted per year $\dot{M}(r)$ interior to a given radius r which is simply computed from $\dot{\rho}$ by the relation

$$\dot{M}(r) = \int_0^r 4\pi r'^2 \dot{\rho}(r')\, dr' \tag{14}$$

In the figure, the dark solid line is the mass accretion profile for the cooling time model fit to the data assuming only Galactic absorption. The $\dot{\rho}$ that goes with this profile is shown as the solid line in Figure 25. The three dotted lines correspond to the cooling time

models with the additional radially dependent extra absorption. The uppermost dotted line corresponds to the case where the lifetime of the cluster was taken to be 10^{10} years, the middle line assumes 5×10^9 years, and the lowest line corresponds to the case with 10^9 years. We first note, as we expect, that the dotted lines do not indicate a significantly different mass accretion rate relative to the case with only Galactic absorption. This makes sense because we had previously found that the density and temperature profiles in the two sets of fits are very similar and the qualitative natures of the fits are also very similar. Now, the dotted lines lie above the solid line because a larger emission must be generated by the model in the case where the absorption is higher. The higher emission is achieved, in part, by having a higher mass accretion rate. Furthermore, for the very same reason, the case with the higher amount of extra absorption should also have the highest mass accretion rate, which we see is indeed the case here.

The short dashed line gives the mass accretion rate in the case of the flattened power law model fit to the data. This mass accretion rate falls well below the plots corresponding to the cooling time model and does not rise above about 1 $M_\odot$/yr. This property can be understood initially by noting that the corresponding $\dot{\rho}$, which is shown as the solid line of Figure 26, drops off very quickly at large radius. As we stated above, this property of $\dot{\rho}$ is the reason that the fluxes of the low temperature lines of the FPCS are underproduced. The low amount of emission coming from the cooling gas is not sufficient to boost the predicted FPCS lines fluxes so that the data can be fit. This now also reflects itself in the very low mass accretion rate predicted for this case. In addition, as a generalization, we can understand the inadequacy of models that have very low mass accretion rates. Specifically, a low mass accretion rate necessarily implies insufficient emission for the FPCS lines to be adequately produced and hence implies that the corresponding model does not represent and accurate picture of the cluster gas. Of, there is the possibility that a low mass accretion rate can be reconciled with the data once other potential sources of heat, such as thermal conduction, are considered. However, we will not consider these possibilities here. Recall that in TB we did consider the possible effects of thermal conduction with regard to the computation of the mass accretion rate but in the present context of a multiphase model the situation becomes considerably more complex because the flow of heat between the ambient medium and the cooling blobs becomes difficult to model.

We end this section by comparing our results to previous determinations of the mass accretion rate. The dots in Figure 26 give the mass accretion profile as determined by Stewart et al. (1984). We see that at radii larger than about 10′ the agreement with our preferred case of the cooling time model is very good and indicates a mass accretion rate of about 10 $M_\odot$/yr at a radius of about 10′. The agreement, however, breaks down at smaller radii, especially at radii less than about 5′. This latter fact is easy to understand if we refer back to Figures 6 and 7 of TB. Here we showed that because Stewart et al. used the old HRI effective area and the old IPC data, their predicted HRI surface brightness profiles was actually too big by about a factor of 2. We would then expect that their mass accretion rates at the radii where the HRI data are taken will be higher than ours, which is indeed the case. Now, other determinations of the mass accretion rate have been made based on data from the FPCS (Canizares et al. 1982), from which a value of about 1.6 $M_\odot$/yr is derived (the value is rescaled to our assumed distance to M87) and the SSS (Mushotzky and Szymkowiak 1988) from which we get a value of about 2.3 $M_\odot$/yr (again rescaled to our assumed distance to M87). If we again refer to Figure 26, we see that we have rough agreement of our preferred case with these values in that our mass accretion rate in the region of the FPCS and SSS fields of view are comparable to the above quoted values. Of, we cannot make a direct comparison of our results because the FPCS and SSS determinations represent emission weighted "averages" over the instrument fields of view whereas we determine the mass accretion rate as a function of radius. Finally, the mass accretion rate was also determined by White & Sarazin (1988) who get values of around 11 $M_\odot$/yr at a radius of 10′ which we can see is again very close to our value. The mass accretion rate profile found by these authors is, however, different than ours, which can be determined by comparing our Figure 26 with Figure 4 of White and Sarazin. This difference can be explained in terms of the different ways in which the parameter q is treated. We have considered it to be a constant with radius, whereas White and Sarazin treat it as a function of radius. Our comparisons to previous work can therefore be summarized as the conclusion that, at least in qualitative terms, the mass accretion rate determination of past workers is consistent with our values. Where differences do occur, the discrepancies can be easily understood in terms of properties of the fit.

We end by emphasizing that our present mass accretion rate determinations represent improvements on the previous work that we have reviewed in the previous paragraph. The

profiles for $\dot{M}$ that we have derived result from a fully self consistent analysis of the emission from the gas which takes into account all of the available data on the cluster. Specifically, with the assumption of a cooling time multiphase model, we have computed the emission from this model and, by comparing to all of the available data and using the most up to date instrument parameters, have derived a model that reproduces reasonably well this data. Using $\dot{\rho}$ derived in this manner, we have then computed $\dot{M}$. In contrast to this, for example, the determination of $\dot{M}$ by Stewart et al. (1984) does not take into account emission from a cooling phase and does not use the revised instrument parameters and data. Furthermore, $\dot{M}$ was computed using a relation that attributed all of the emission to isobarically cooling gas which is not consistent with the initial exclusion of emission from a cooling component in the computation of the emission from the model. Also, line emission data from the FPCS is not well fit by the model. As for the FPCS determination of $\dot{M}$, only this line emission data were used to derive an average mass accretion rate over the instrument field of view. Similarly, the SSS determination uses data only from the SSS. Finally, we have discussed rather extensively in the Introduction the shortcomings in the work of White & Sarazin (1988) from the standpoint of the modelling of the emission. The resulting uncertainty will also reflect itself as an uncertainty in the predicted mass accretion rates. We have now found that despite the problems that we have just discussed with the previous determinations of $\dot{M}$, for this one property of the cluster, previous workers have gotten values that are consistent, at least qualitatively, with the our present determinations.

VI. CONCLUSIONS

We now summarise the conclusions of this paper. We have considered two classes of multiphase models for the intracluster gas around M87. First, we considered the cooling time model of White & Sarazin (1987a) in which mass dropped out of the ambient intracluster medium at a rate specified locally by the gas cooling time. In addition, we considered an *ad hoc* model where the rate at which mass dropped out of the flow was determined by a simple power law profile (later modified to include the possibility of a flattened center). We have found that although the data itself (especially the HRI data and the optical mass determinations) make it somewhat difficult to exactly quantify the goodness of fit of our

models to the data, nevertheless, we are able to draw some conclusions in this regard. First, we find that the inclusion of a cooling phase in the manner of the cooling time model in addition to an ambient phase improves upon the fit to the data relative to that with only the ambient non–cooling phase in an important manner. It was shown in TB, and elaborated upon in the present work, that a single phase medium was inadequate for explaining all of the available data on M87. Specifically, a single phase model that fits all of the X–ray data (again excluding the SSS for reasons that we will summarise below) will not provide a good agreement with optically determined mass data. Stated another way, in order for a single phase model to produce adequate emission to fit the X–ray data, especially the the observed low temperature emission, low temperatures below about 10^7 °K are indicated. This, however, through the equation of hydrostatic equilibrium implies a mass profile that is too low at small radius to agree with the optical determinations. The addition of a cooling phase of the cooling time variety solves this problem by effectively increasing the line emissivity of the low temperature lines at high temperatures. Therefore, sufficient emission can then produced at high temperatures to accomadate the data on the low temperature lines. At the same time, the higher temperatures enable consistency of the predicted mass profiles with the optical determinations. The existence of a multiphase medium for the gas around M87 is therefore strongly indicated by the data.

The situation when a power law cooling component was included was rather different than in the previous case. First, it was found that the best fit power law for $\dot{\rho}$ does not have a slope of -2 which corresponds to the canonical mass accretion rate of $\dot{M}(r) \sim r$. Rather, the best fit case has a slope of -3.5, which is steeper. With regard to the goodness of the fit, the improvement in the fit over the single phase case that was obtained when the cooling time model was assumed is not achieved with the present models. The reason that this occurs is that the power law drops off so fast with radius that only the emission in the very central regions is enhances by the inclusion of a power law cooling component. The region where most of the line emission as seen by the FPCS originates lies outside of this inner, enhanced region. We therefore conclude that a power law model is not a good representation of the M87 cooling flow.

We stated in the introduction that we were also going to use our fits to the data as a tool to try to confirm the findings of White et al. (1991) that extra absorption above the Galactic value was indicated. We first tested this by uniformly increasing the

assumed column density by the amount quoted by White et al. and making a fit to the data assuming the cooling time model. We found that although the simultaneous fit to the HRI, IPC, and FPCS was indeed improved (almost all of the improvement came in the HRI part of the data), the requirement that the predicted equivalent width of the 7 keV Fe line complex must also fit the measured value of about 1 keV implied unreasonably high metal abundances (e.g. an oxygen abundance of 24 times the solar value). This implied that the fit was not improved in a realistic manner. Furthermore, since White et al. found that the extra column density was required to fit the SSS data, we also predicted the SSS spectrum for the cooling time model both with only Galactic absorption and with the uniformly distributed extra absorption. We found that in both cases, the SSS spectra were relatively well fit at energies above about 1.2 keV. However, the spectrum was overproduced at around 0.65 keV, where the OVIII Lyα line fluoresces, and underpredicted at around 1 keV, where the Fe L lines fluoresces. Therefore, contrary to the results of White et al., whose conclusions are based solely on data from the SSS, we found that the inclusion of extra absorption uniformly distributed across the cluster and a cooling time cooling component did not improve upon the fit to the SSS, especially at low energies where the improvements were supposed to occur. We further examined the case where the extra absorption itself arrises out of the gas that cools and condenses out of the flow and therefore produces a radially dependent extra column density. In this case we found that the fits to the data where basically the same as the case where only Galactic absorption is assumed in both its properties and in the goodness of fit. This occurred because the amount of deposited material did not represent enough absorption to be noticed above the Galactic component at most radii. It was only at the innermost radii where the added absorption had any effect. The data, therefore, do not place restrictions upon the amount of accreted gas that could have gone into absorbing gas because it would hardly be noticeable anyway. As for the SSS, the predicted spectrum in this case was again identical to that corresponding to the case with only Galactic absorption. We conclude therefore that extra absorption above the Galactic value is not indicated by either the data from the SSS or data from the other *Einstein* instruments.

In the course of the work on the extra absorption, we were able to understand the lack of a good fit to the SSS of our models as an apparent inconsistency between the measurements of the SSS and the FPCS. This conclusion came from the argument that if

the SSS and the FPCS are observing basically the same gas (which is the case in our fits), and if the FPCS line flux in a given energy range is well fit, then so too must the SSS spectrum in that same energy range. As it turns out, the constraint from the OVIII Lyα line as observed by the FPCS implies that the emission at an energy of around 0.65 keV in the SSS be about twice as high as is observed. This discrepancy cannot be understood as a consequence of poor modelling since if the same gas is observed by two instruments, the conclusion that a good fit to one instrument necessarily implies a good fit to the other is inescapable. The discrepancy at around 1 keV, on the other hand, can be potentially explained as arising out of problems with the atomic emissivity computations, but, again we argued that this too could not explain away the disparity at around 0.65 keV. We then commented upon the various possible solutions for the discrepancy between the two instruments and further discovered that even without data from the FPCS, there was a problem between the SSS and the HRI, which also views the innermost regions of the cluster. Specifically, if Galactic absorption is first assumed, the high amount of emission required by the HRI also implies some overprediction of the SSS spectrum around 0.65 keV. If the absorbing column density is increased to the value as quoted by White et al. (1991), we find that the spectrum at around 0.65 keV can now be made to agree with the data, but that the spectrum at higher energies gets overproduced in order to generate enough HRI emission to fit the data. We also note that in spectral work on the supernova remnant N132D (Hwang, Canizares, Markert, & Hughes 1992; preprint), it was found that the ionization timescales as determined from the OVIII Lyα lines of the FPCS and the SSS were also discrepant by about a factor of two in the same sense that we have found. That is, the consistency of ionization timescales as determined from FPCS data and SSS data require that the SSS see about twice as much emission as is observed. This conclusion is telling since the modelling for N132D is very different from that which was performed in this paper. For example, we have assumed ionization equilibrium in computing the emission out of our cluster models whereas the N132D modelling was performed without this assumption. In conclusion, therefore, although we have described and understood the nature of the problem that exists between the FPCS and the SSS, we do not have the means to further address it here. The fact of this potential problem with the SSS should cast considerable doubt upon conclusions that are based solely upon SSS data, for example the claim of extra absorption in the M87 cluster gas. We emphasize, however,

that we make no statement concerning the other conclusions of the paper of White et al. (1991) with regard to extra absorption in other clusters.

Finally, we have computed the mass accreted within a given radius as a function of radius and found that our results are basically consistent with past determinations based on subsets of the entire data set that we have considered. Departures from our results in the case of the determination of Stewart et al. (1984) were understood in terms of differences in the modelling of the cluster. If additional sources of heat, such as thermal conduction, are ignored, we find a mass accretion rate of about 10 $M_{\odot}$/yr at a radius of about 10′ for our best fit cooling time model. We also found that our power law models gave a very low mass accretion rate which was a refection of the production of insufficient amounts of emission for the low temperature FPCS lines. This latter model serves as an example of a case where a mass accretion rate that is too low does not produce enough emission for the data to be explained.

As for future work on the M87 cluster, we stated that several aspects remain to be well understood. From the standpoint of our models themselves, we saw that the optical mass determinations and the HRI data were difficult to use. In the case of the optical mass constraints this was because of the discrepant determinations based on spectroscopic work and globular cluster work. In this regard, we can get a better sense of how well our models actually fit the mass data if the determinations were to be refined. With respect to the HRI, problems with the assignment of various components of the emission to various emission processes (especially for the component morphologically similar to the radio halo) and the non–spherically symmetric nature of the innermost emission present difficulties. Observations with the new, more sensitive X–ray instruments on satellites such as AXAF or ASTRO-D will help to resolve these issues although we don't expect our conclusions to be modified based on our discussion where we examined the consequences of varying the data. In addition, the uncertainty of what exactly is the temperature of the gas in the region around 10′ can be addressed by new observations, especially with ASTRO-D. Again, we do not expect changes in this temperature to change our conclusions.

Gratitude is expressed to C. Canizares for many discussions and the suggestion that we investigate the models of White and Sarazin. We also thank D. Fabricant for his many helpful conversations with the authors and J. Hughes for discussions on the SSS. This work was supported by NASA grant number ~~NAG~~. NAG 5 -1355.

REFERENCES

Allen, C. W. 1973, Astrophysical Quantities, (London: Athlone Press).

Bertschinger, E. 1989, ApJ, 340, 666.

Canizares, C. R., Clark, G. W., Jernigan, J. G., & Markert, T. H. 1982, ApJ, 262, 33.

Edge, A. C., Stewart, G. C., & Smith, A. 1988, in Hot Thin Plasmas in Astrophysics, ed. Pallavicini, R., (Dordrecht: Kluwer), p.335.

Fabian, A. C., Hu, E. M., Cowie, L. L., & Grindlay, J. 1981, 248, 47.

Fabricant, D. & Gorenstein, P. 1983, ApJ, 267, 535.

Fabricant, D., Lecar, M., & Gorenstein, P. 1980, ApJ, 241, 552.

Feigelson, E. D., Wood, P. A., Schreier, E. J., Harris, D. E., & Reid, M. J. 1987, ApJ, 312, 101.

Giacconi, R., et al. 1979, ApJ, 230, 540.

Harris, D. E. (ed.) 1984, Einstein Observatory Revised Users' Manual, Harvard Smithsonian Center for Astrophysics.

Huchra, J., & Brodie, J. 1987, AJ, 93, 779.

Koyama, K., Takano, S., Tawara, Y. 1991, Nature, 350, 135.

Lea, S. M., Mushotzky, R., & Holt, S. S. 1982, ApJ, 262, 24.

Mould, J. R., Oke, P. T., & Nemec, J. M. 1987, AJ, 92, 53.

Mushotzky, R. F., Serlemitsos, P. J., Smith, B. W., Boldt, E. A., & Holt, S. S. 1978, ApJ, 225, 21.

Mushotzky, R. F., & Szymkowiak, A. E. 1988, in Cooling Flows in Clusters of Galaxies, ed. Fabian, A. C., (Dordrecht: Kluwer),p.53.

Rothenflug, R., & Arnaud, M. 1985, A&A, 144, 431.

Sargent, W. L. W., Young, P. J. Boksenberg, A., Shortridge, K., Lynds, C. R., & Hartwick, F. D. A. 1978, ApJ, 221, 831.

Schreier, E. J., Gorenstein, P.,Feigelson, E. D. 1982, ApJ, 261,42.

Serlemitsos, P. J., Smith, B. W., Boldt, E. A., Holt, S. S., & Swank, J. H. 1977, ApJ, 211, L63.

Schattenburg, M. L., Canizares, C. R., Berg, C. J., Clark, G. W., Markert, T. H., & Winkler, P. F. 1980, ApJ, 241, L151.

Schattenburg, M. L., Canizares, C. R. 1986, ApJ, 301, 759.

Stewart, G. C., Canizares, C. R., Fabian, A. C., & Nulsen, P. E. J. 1984a, ApJ, 278, 536.

Thomas, P. A., Fabian, A. C., & Nulsen, P. E. J. 1987, MNRAS, 228, 973.

White, D. A., Fabian, A. C., Johnstone, R. M., Mushotzky, R. F., & Arnaud, K. A. 1991, MNRAS, 252, 72.

White, R. E., & Sarazin, C. L. 1987a, ApJ, 318, 612.

White, R. E., & Sarazin, C. L. 1987b, ApJ, 318, 621.

White, R. E., & Sarazin, C. L. 1988, ApJ, 335, 688.

FIGURE CAPTIONS

FIGURE 1: Density profiles. The dotted line gives the density profile in a single phase fit to the data, including the mass constraints, assuming that $T_\infty = 3.8 \times 10^7$ °K. The corresponding cooling time multiphase fit is given as the solid line. The short dashed line gives the density in a cooling time multiphase fit assuming that $T_\infty = 6 \times 10^7$ °K.

FIGURE 2: Temperature profiles. The dotted line gives the temperature for the single phase fit to the data, including the mass constraints, assuming that $T_\infty = 3.8 \times 10^7$ °K. The corresponding multiphase fit is given as the solid line. The cooling time multiphase fit with $T_\infty = 6 \times 10^7$ °K is given as the short dashed line.

FIGURE 3: Density profiles. The dotted line gives the density for the single phase fit with the temperature constraint at 10′. The corresponding cooling time multiphase fit is given as the solid line.

FIGURE 4: Temperature profiles. The dotted line gives the temperature for the single phase fit with the temperature constraint at 10′. The corresponding cooling time fit is given as the solid line. The dashed dotted line (same as the solid line of Figure 2) is shown for ease of comparison and gives the temperature for the cooling time multiphase fit with $T_\infty = 3.8 \times 10^7$ °K.

FIGURE 5: HRI surface brightness profiles. The HRI data are plotted as the data points. The dotted line gives the predicted surface brightness distribution for the single phase fit with the temperature constraint at 10′. The corresponding cooling time multiphase fit is given as the solid line.

FIGURE 6: IPC surface brightness profiles. The IPC data are plotted as the data points. The dotted line gives the predicted surface brightness distribution for the single phase fit with the temperature constraint at 10′. The corresponding cooling time multiphase fit is given as the solid line.

FIGURE 7: FPCS residuals. We plot here the residuals (the observed values minus the predicted values divided by the error) due to the FPCS lines. Line numbers on the abscissa correspond to observed FPCS lines and line blends. Number 1 corresponds to

OVIII Lyα, 2 to 7 correspond to blends 1 to 6, respectively, and 8 corresponds to the FeXVII line. The total contribution to χ^2 appears on the lower right hand side of each panel. The various cases plotted are: (a) the single phase fit to the data assuming the temperature constraint at 10′; (b) The corresponding cooling time multiphase fit.

FIGURE 8: Mass profiles. We plot here the predicted mass profiles for some of our models along with optically derived values. The data points are the determinations of Sargent et al. (1978), the single square data point is the mass determination of Huchra & Brodie (1987), and the heavy solid line is the determination due to Mould et al. (1987). The dotted line gives the mass corresponding to the single phase fit with the temperature constraint at 10′. The corresponding cooling time multiphase mass profile is given as the light solid line. The dashed dotted line gives the mass profile corresponding to a single phase fit to only the X-ray data (no mass constraints) which is reproduced from TB for comparison.

FIGURE 9: SSS spectra. The SSS data from a central pointing of M87 are given as the daggers. The light histogram gives the predicted spectrum due only to thermal emission in the cooling time multiphase fit with the temperature constraint at 10′. The dark histogram gives the total predicted SSS spectrum for the same case, including emission from a central power law source.

FIGURE 10: Density profiles. The solid line gives the density profile for the cooling time fit assuming that the column density is $1.75 \times 10^{21}\mathrm{cm}^2$ (following White et al. (1991)) distributed uniformly with projected radius. The other lines give the density for the fits where the extra absorption is computed self consistently using eq. (10) of the text. Specifically, the dotted line gives the case where t_{max} is 10^9 years, the short dashed line is when t_{max} is 5×10^9 years, and the long dashed line is when t_{max} is 10^{10} years.

FIGURE 11: Temperature profiles. The solid line gives the temperature profile for the cooling time multiphase fit assuming that the column density is $1.75 \times 10^{21}\mathrm{cm}^2$ distributed uniformly with projected radius. The other lines give the temperature for the fits with self consistently computed extra absorption. The dotted line gives the case where t_{max} is 10^9 years, the short dashed line is when t_{max} is 5×10^9 years, and the long dashed line is when t_{max} is 10^{10} years.

FIGURE 12: HRI surface brightness profiles. The solid line gives the predicted HRI surface brightness for the cooling time multiphase fit assuming an absorbing column density of $1.75 \times 10^{21}\mathrm{cm}^2$. The other lines give the surface brightness for the fits with self consistently computed extra absorption. The dotted line gives the case where t_{max} is 10^9 years, the short dashed line is when t_{max} is 5×10^9 years, and the long dashed line is when t_{max} is 10^{10} years.

FIGURE 13: IPC surface brightness profiles. The solid line gives the predicted IPC surface brightness for the cooling time multiphase fit assuming an absorbing column density of $1.75 \times 10^{21}\mathrm{cm}^2$. The other lines give the surface brightness for the fits with self consistently computed extra absorption. The dotted line gives the case where t_{max} is 10^9 years, the short dashed line is when t_{max} is 5×10^9 years, and the long dashed line is when t_{max} is 10^{10} years. All of the lines lie so closely to each other that they are all essentially overlie each other.

FIGURE 14: FPCS residuals. Panel (c) gives the residuals for the cooling time multiphase fit where the column density is assumed to be $1.75 \times 10^{21}\mathrm{cm}^2$. Panel (d) corresponds to the fit with a self consistently computed column density with t_{max} assumed to be 10^{10} years. Panel (e) gives the results for the case where t_{max} is assumed to be 5×10^9 years and panel (f) is for the case where t_{max} is 10^9 years.

FIGURE 15: Mass profiles. The solid line gives the mass profile for the cooling time multiphase fit where the column density is assumed to be $1.75 \times 10^{21}\mathrm{cm}^2$. The dotted line, short and long dashed lines (which overlie the solid line) correspond to the cases with self consistent computed extra absorption.

FIGURE 16: SSS spectrum. The predicted spectrum of the thermal thermal emission for the cooling time multiphase fit with a column density of $1.75 \times 10^{21}\mathrm{cm}^2$ is given as the light solid line. The dark solid line gives total spectrum including the emission from the central point source (assumed to be a power law).

FIGURE 17: Distribution in temperature of the emission as seen by the FPCS. These plots gives the the amounts of emission as seen by the FPCS as a function of the temperature of the gas. The dark solid line corresponds the the OVIII Lyα line and the

light solid line corresponds to the the FeXVII line. The other lines correspond to the various Fe L blends.

FIGURE 18: SSS spectrum. These are the predicted SSS spectra in the cooling time multiphase fits to the data excluding that of the FPCS. The light solid histogram corresponds to the case where only Galactic absorption is assumed. The dark histogram gives the spectrum in the case that the column density is assumed to be $1.75 \times 10^{21}\mathrm{cm}^2$.

FIGURE 19: Absorbing column densities. The light solid horizontal line indicates the level of Galactic absorption. The dark solid line gives half of the total column density through the cluster that would have accumulated in a time of 10^{10} years assuming that the best fit cooling time multiphase model with Galactic absorption. The other lines give half of the total column density in the cases where the extra absorption is computed self consistently. The dotted line corresponds to the case where t_{max} is assumed to be 10^9 years, the short dashed line corresponds to the case where t_{max} is 5×10^9 years, and the long dashed line has a t_{max} of 10^{10} years.

FIGURE 20: Density profiles. The dark solid line gives the density of the best fit power law multiphase model with Galactic absorption. The dotted line is the best fit density for the power law multiphase model with an absorbing column density of $1.75 \times 10^{21}\mathrm{cm}^2$.

FIGURE 21: Temperature profiles. The dark solid line gives the temperature of the best fit power law multiphase model with Galactic absorption. The dotted line is the best fit temperature for the power law multiphase model with an absorbing column density of $1.75 \times 10^{21}\mathrm{cm}^2$.

FIGURE 22: HRI surface brightness distribution. The dark solid line corresponds to the best fit power law multiphase model with Galactic absorption. The dotted line is for the best fit power law multiphase model with column density of $1.75 \times 10^{21}\mathrm{cm}^2$.

FIGURE 23: IPC surface brightness distribution. The dark solid line corresponds to the best fit power law multiphase model with Galactic absorption. The dotted line is for the best fit power law multiphase model with column density of $1.75 \times 10^{21}\mathrm{cm}^2$.

FIGURE 24: FPCS residuals. Panel (g) gives the FPCS residuals for the best fit power law multiphase model with Galactic absorption. Panel (h) gives the case where the column density is increased to $1.75 \times 10^{21}\mathrm{cm}^2$.

FIGURE 24: $\dot{\rho}$ profiles. The solid line gives $\dot{\rho}$ for the best fit cooling time multiphase model assuming Galactic absorption. The dotted line gives $\dot{\rho}$ for the best fit power law multiphase model assuming Galactic absorption and the short dashed line gives $\dot{\rho}$ for the best fit flattened power law model with Galactic absorption.

FIGURE 25: $\dot{M}(< r)$ profiles. The dots give the determinations of $\dot{M}$ by Stewart et al. (1984). The dark solid line gives $\dot{M}$ for the best fit cooling time multiphase model assuming Galactic absorption. The dotted lines correspond to the cooling time multiphase models with self consistently computed extra absorption. The uppermost dotted line has t_{max} of 10^{10} years, the middle dotted line has t_{max} of 5×10^9 years, and the bottom line has t_{max} of 10^9 years. The short dashed line give $\dot{M}$ computed with the best fit flattened power law multiphase model.

TABLE 1

Case[†]	a_1(kpc)	$n_0(10^{-3}\mathrm{cm}^{-3})$	a_2(kpc)	α_2	q or N_{mult}	$N(10^{20}\mathrm{cm}^2)$
a..	7.39	4.85	1.68×10^5	0.170	—	2.5
b..	6.63	4.31	4.58×10^4	0.114	0.874	2.5
c..	5.73	4.79	6.53×10^{16}	0.128	1.64	17.5
d..	6.04	5.06	1.30×10^9	0.140	0.748	2.5[a]
e..	6.11	4.98	7.51×10^{15}	0.138	0.751	2.5[a]
f..	6.26	4.79	1.97×10^{12}	0.133	0.770	2.5[a]
g..	7.55	4.63	2.83×10^{16}	6.68×10^{-2}	2.95×10^{-41}[b]	2.5
h..	6.84	5.05	1.15×10^{16}	8.53×10^{-2}	5.15×10^{-41}[c]	17.5

[†] Case labels are the same as panel labels in figures for FPCS residuals

[a] Additional column density is given as a line of sight integral of equation (10) in text

[b] Units of N_{mult} in this case are $\frac{\mathrm{g}}{\mathrm{cm}^3}$ $(\mathrm{kpc})^{3.5}$

[c] Units of N_{mult} in this case are $\frac{\mathrm{g}}{\mathrm{cm}^3}$ kpc^3

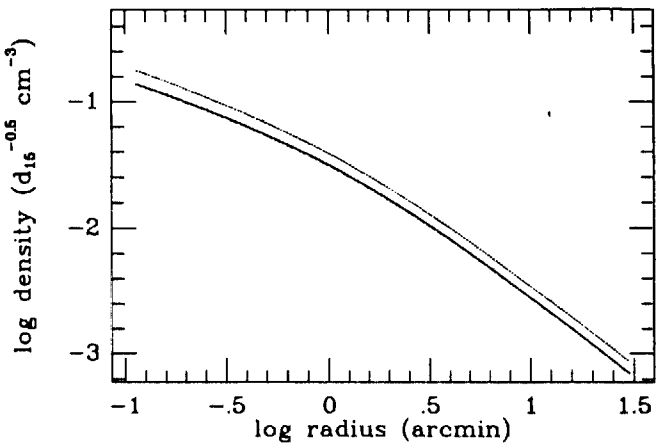

FIGURE 1

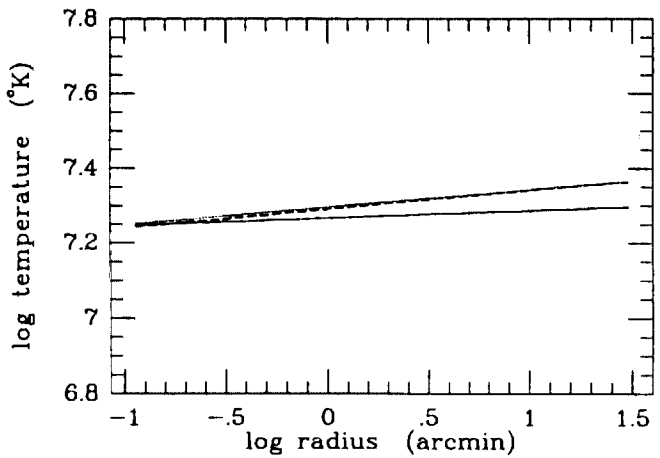

FIGURE 2

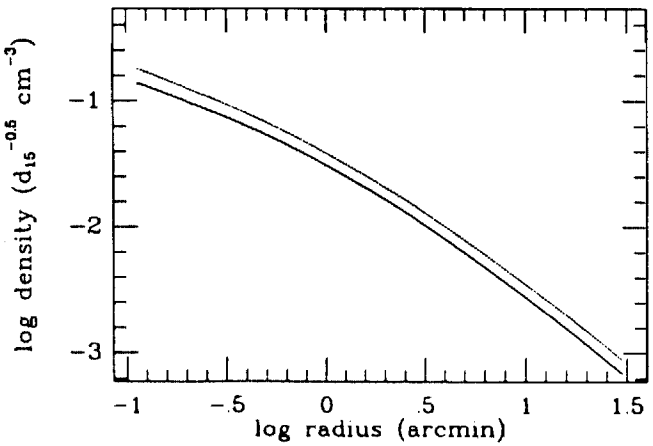

FIGURE 3

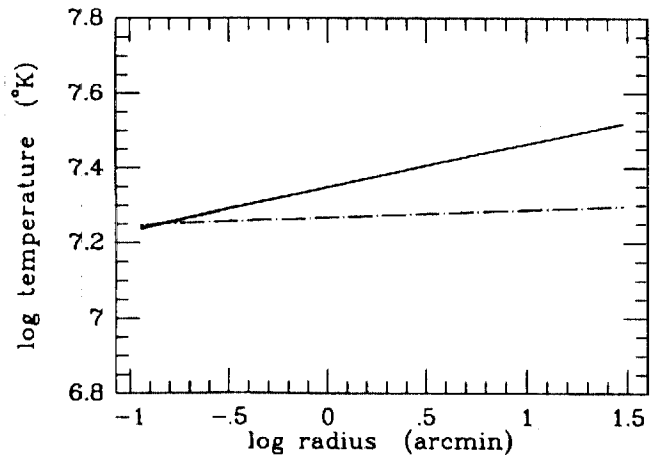

FIGURE 4

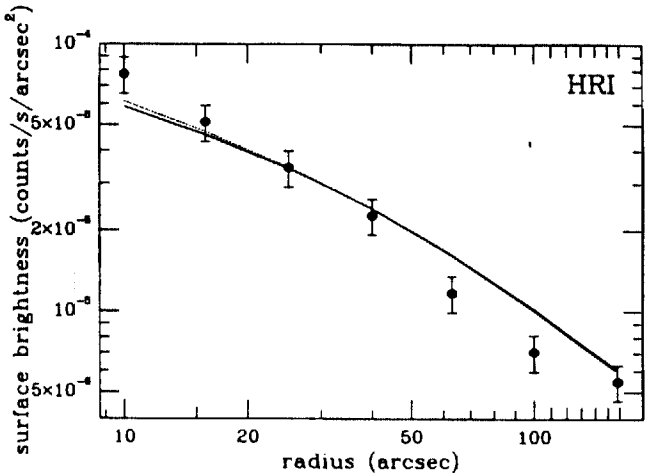

FIGURE 5

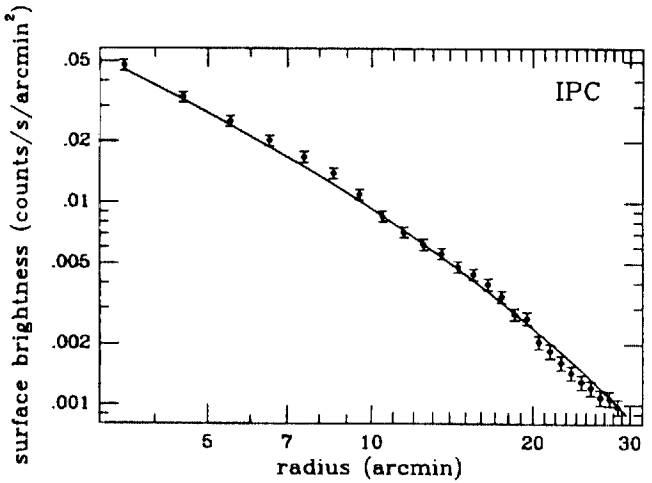

FIGURE 6

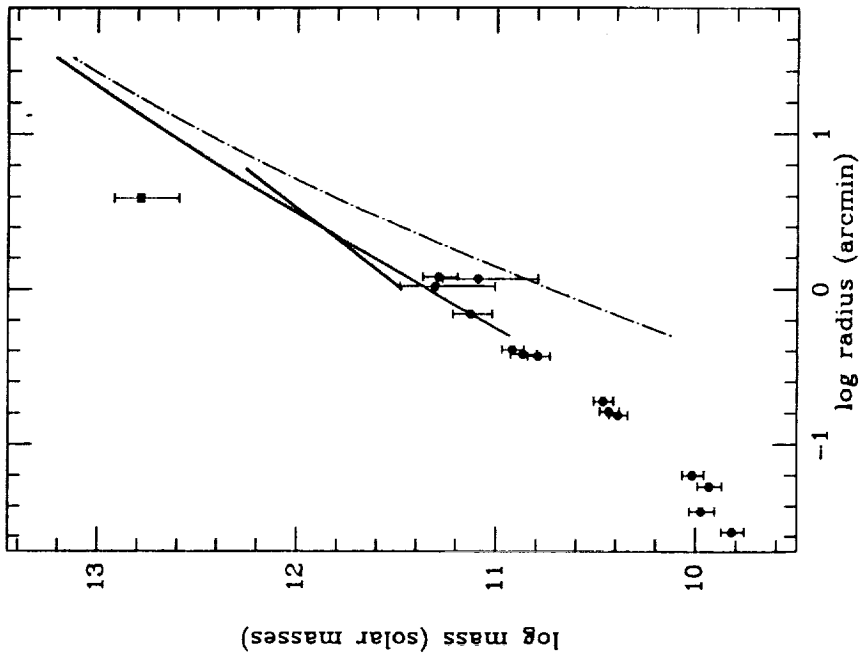

FIGURE 8

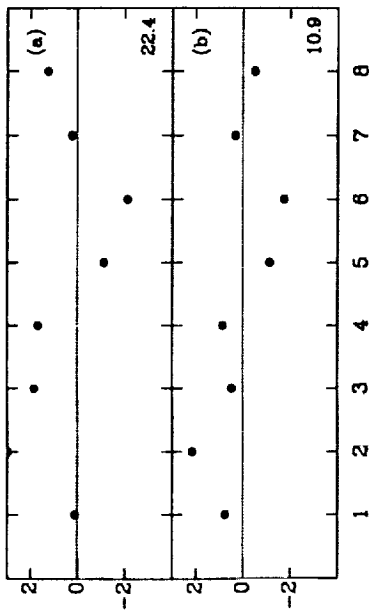

FIGURE 7

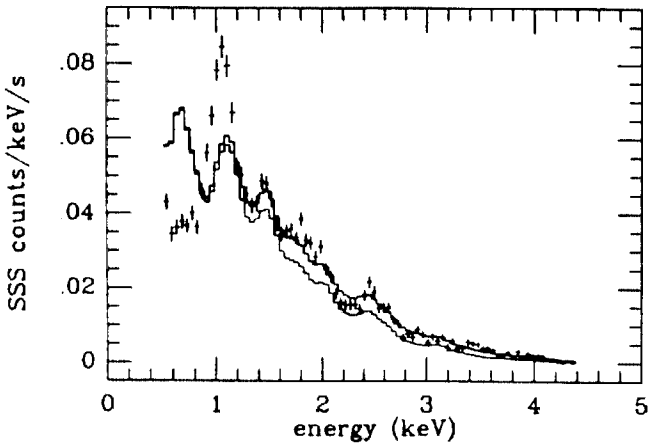

FIGURE 9

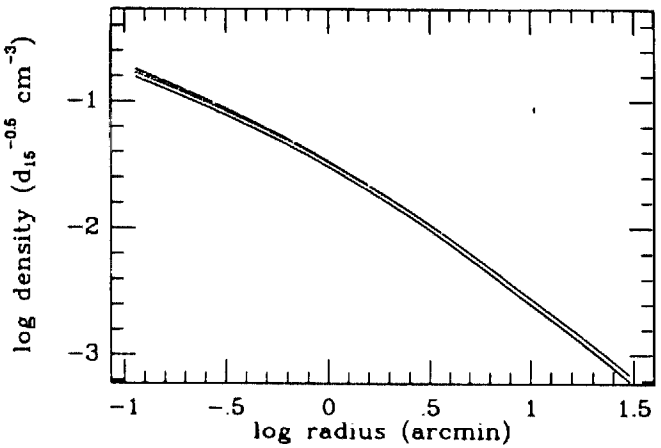

FIGURE 10

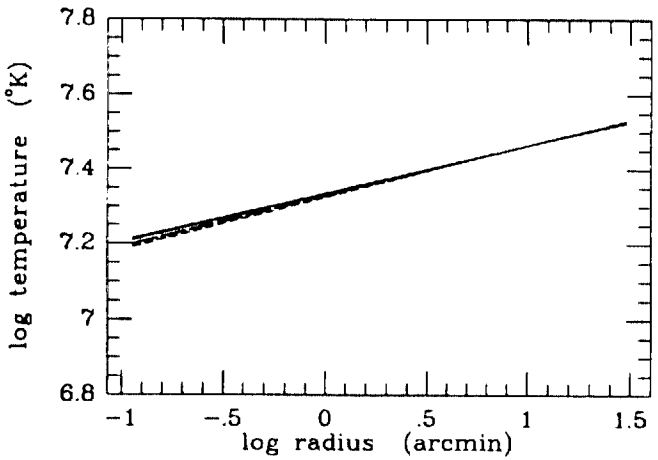

FIGURE 11

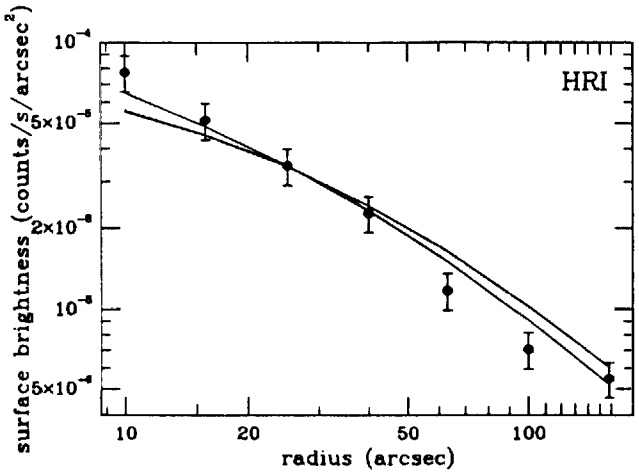

FIGURE 12

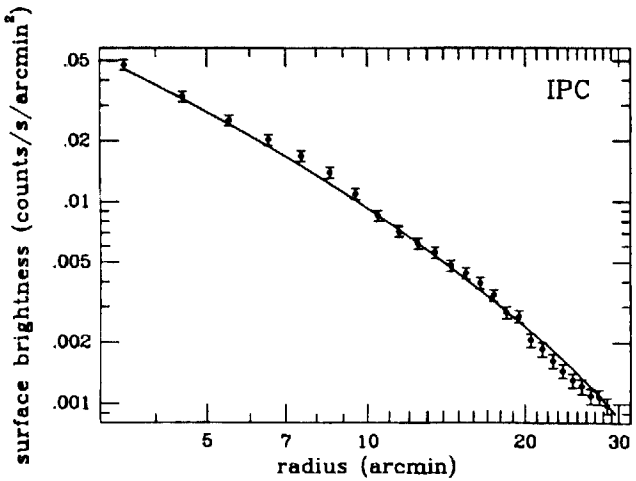

FIGURE 13

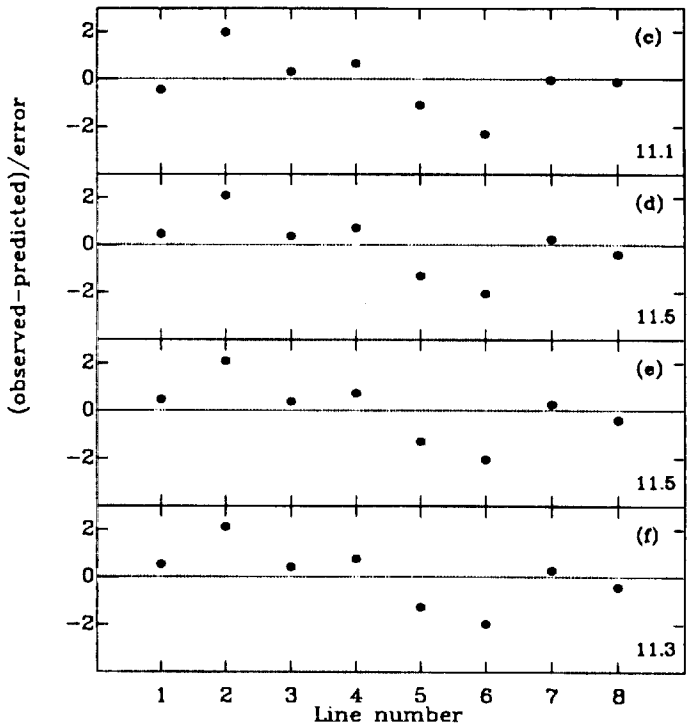

FIGURE 14

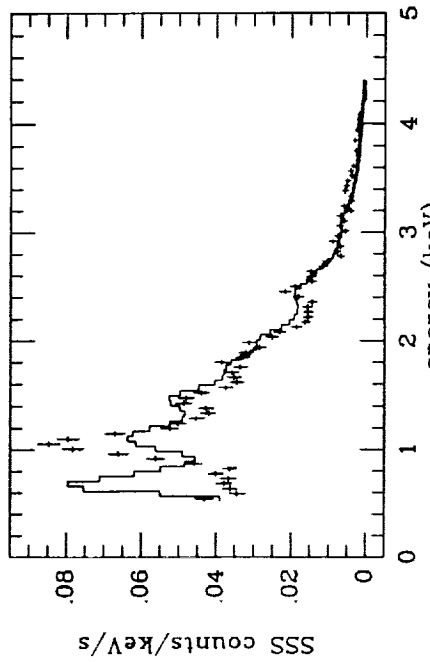

FIGURE 16

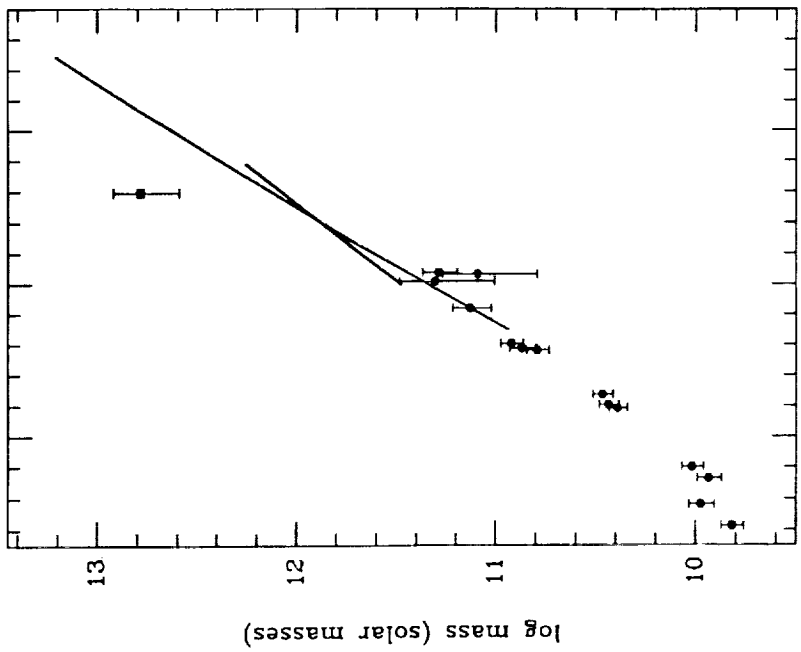

FIGURE 15

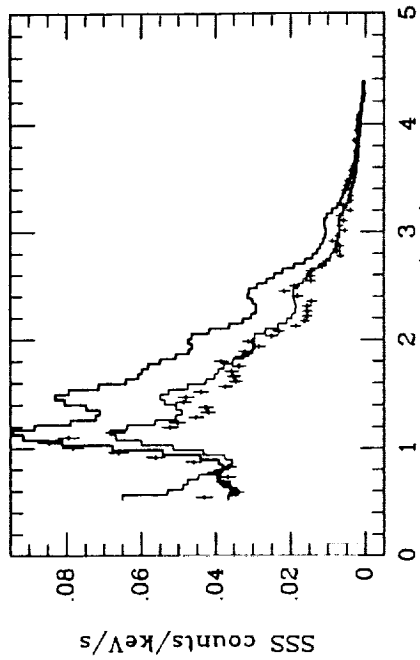

FIGURE 18

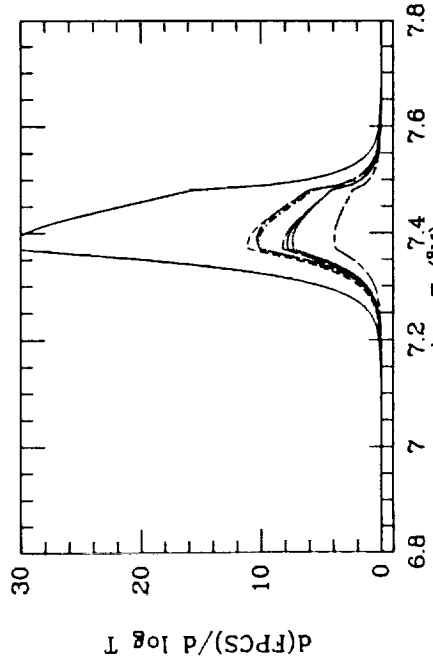

FIGURE 17

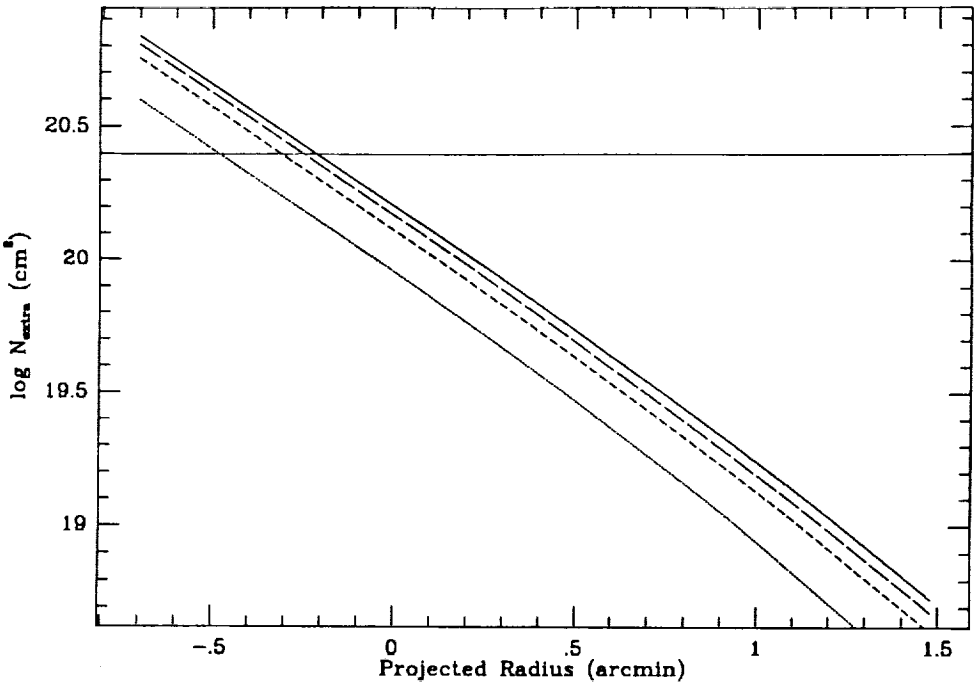

FIGURE 19

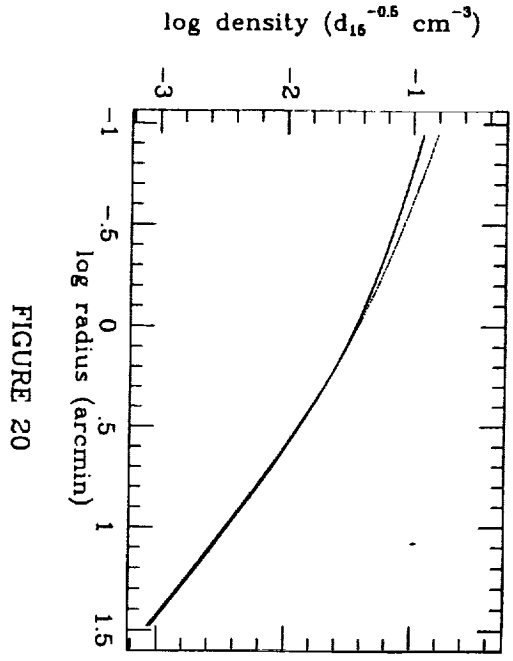

FIGURE 20

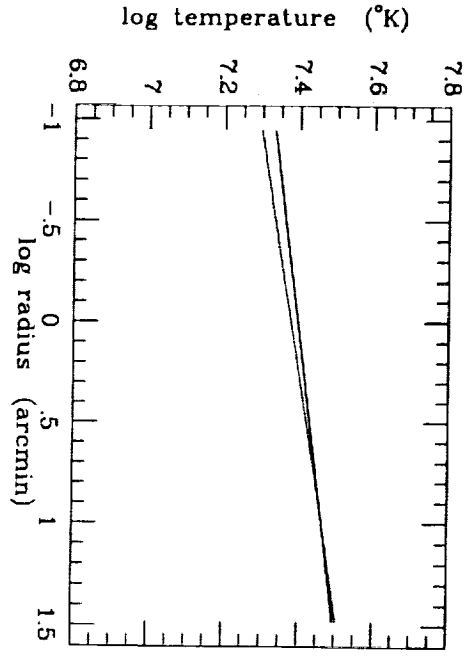

FIGURE 21

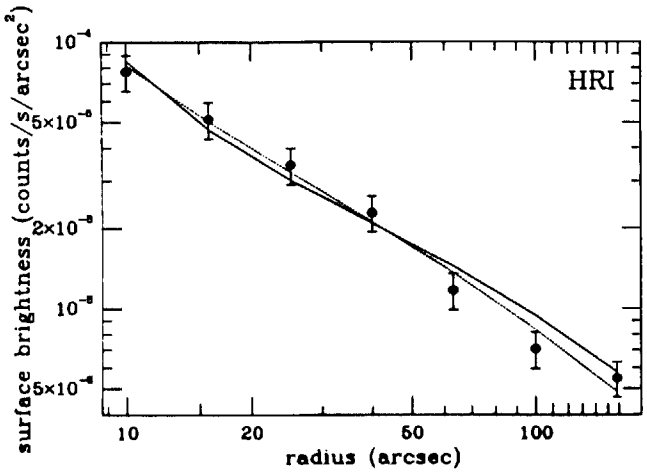

FIGURE 22

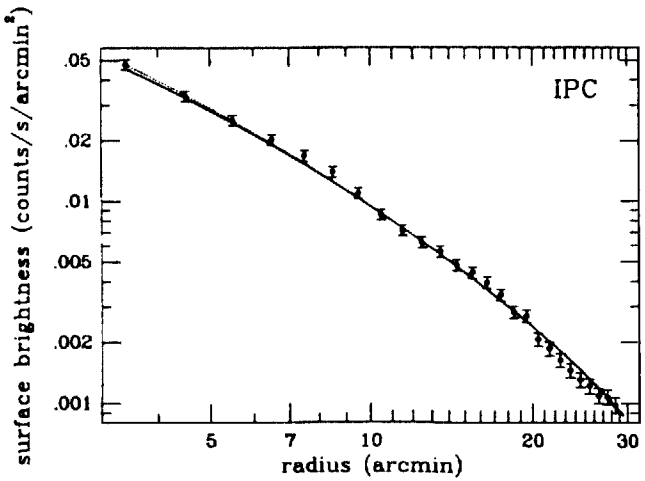

FIGURE 23

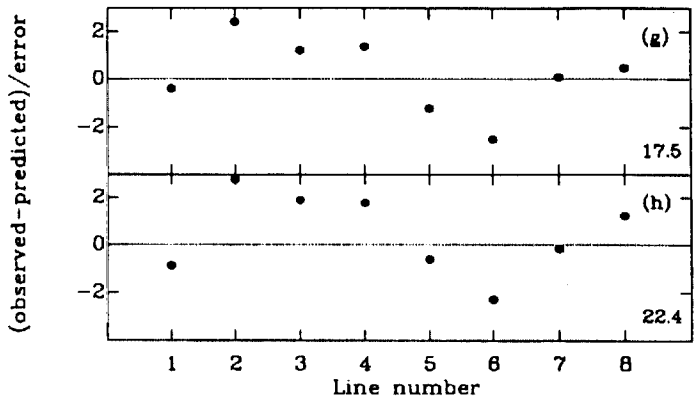

FIGURE 24

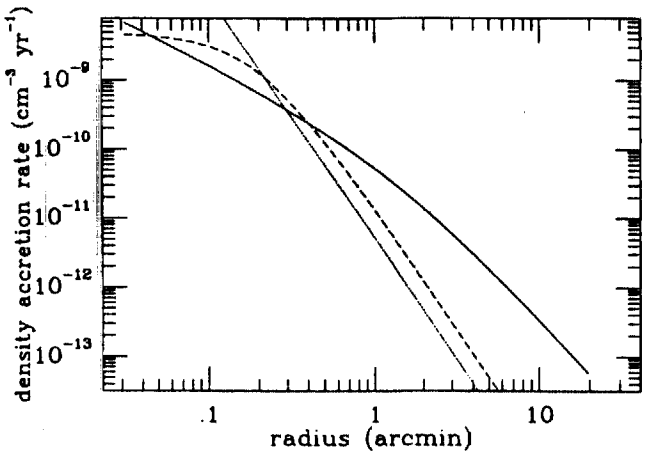

FIGURE 25

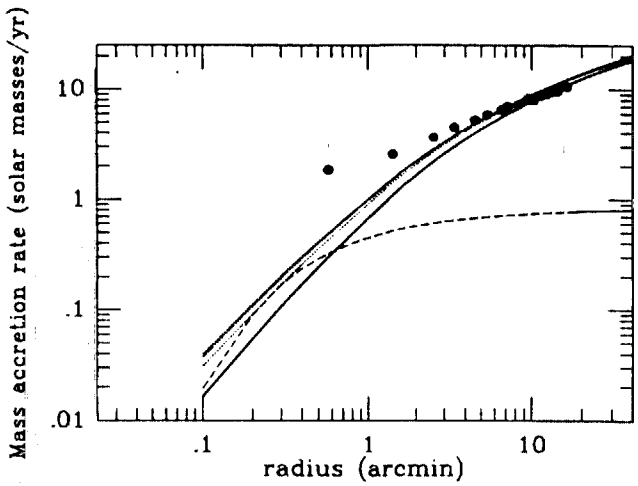

FIGURE 26